Hydrothermal activity along a strike-slip fault zone and host units in the São Francisco Craton, Brazil – Implications for fluid flow in sedimentary basins

Cazarin, C. L.; van der Velde, R.; Santos, R. V.; Reijmer, J. J.G.; Bezerra, F. H.R.; Bertotti, G.; La Bruna, V.; Silva, D. C.C.; de Castro, D. L.; Srivastava, N. K.

DOI
10.1016/j.precamres.2021.106365

Publication date
2021

Document Version
Accepted author manuscript

Published in
Precambrian Research

Abstract

This study combines multiscale analyses of geological, fault, fracture, and stable isotope data to investigate strike-slip deformation and channeling of hydrothermal fluids along the Cafarnaum fault and calcite veins at different distances from the fault, which is a structure in the São Francisco Craton, northeastern Brazil. Meteoric fluids with δD values near -45‰ and $\delta^{18}O$ values near -6.5‰ and temperatures at 40-70°C precipitated as calcite veins in the host carbonate units. The Cafarnaum fault, a N-S-striking vertical, ~170 km long fault zone, juxtaposes Neoproterozoic carbonate rocks in the western block and Mesoproterozoic siliciclastic rocks in the eastern block. A zone of restraining bends occurs at the central part of the fault, whereas termination zones of horsetail geometry occur at both ends of the Cafarnaum fault. These zones are marked by NW-SE-striking extensional faults that are oblique to the main N-S-striking fault zone, where hydrothermal deposits occur. The zone of influence of the Cafarnaum fault is ~20 km wide around the main fault. The fault formed during the Brasiliano orogeny (740-560 Ma) after Neoproterozoic carbonate platform deposition. In contrast with the host units, fluids along the fault zone originated in deeper levels of the crust and show much lower $\delta^{18}O$ values, indicating higher crystallization temperatures. These fluids caused brecciation in the Neoproterozoic carbonate host rocks, whereas a subsequent decrease in fluid pressure and cooling near the surface resulted in the precipitation of a hydrothermal paragenesis in veins, also affecting the host rock.

Keywords: carbonate veins, hydrothermal fluid, strike-slip fault, Salitre Formation, São Francisco Craton

1. Introduction

Sedimentary basins display different fluid migration regimes depending on the host rock, particularly in areas subjected to extensional tectonics. Sedimentary stratified layers may allow basinal fluids to migrate laterally parallel to bedding for hundreds of kilometers (Qing and Mountjoy, 1992). In most instances, sedimentary basins display limited vertical fluid flow due to impermeable layers; hence, fluid conduits cannot connect deep and shallow parts of a basin. Pore water usually has a low-velocity flow regime, and its primary geochemical values are therefore easily altered by reactions with host rock minerals and mixing with other fluids (Bjorlykke and Egeberg, 1993).

Vertical fluid flow pathways in sedimentary basins are associated with fault zones (Haneberg et al., 1999; Hardebeck and Hauksson, 1999). Depending on the structures and/or permeability properties, fault zones can either act as hydraulic barriers or as preferential conduits for geofluid migration (Gudmundsson, 2001; Rawling et al., 2001; Smeraglia et al., 2021; La Bruna et al., 2021). These characteristics are also linked to the several structural/diagenetic phases affecting the carbonate rocks from the earliest diagenetic stages (e.g., La Bruna et al., 2020). In fact, selective cementation and structural diagenetic processes are key factors in fault permeability control (Hausegger et al., 2010; Ngwenya et al., 2000).

Strike-slip faults create complex and heterogeneous permeability anisotropy and strongly influence fluid migration in crustal fault zones (Caine et al., 2010; Bense et al., 2013; Arancibia et al., 2014). A wide variety of processes at various scales can occur during fault growth and lead to a large range of fault architectures and properties that influence fluid flow behavior (Wibberley and

78 Shipton, 2010). The activity of major and weak strike-slip fault systems is
79 influenced by fluid flow (e.g., Byerlee, 1990; Rice, 1992; Sleep and Blanpied,
80 1992; Evans and Chester, 1995; Zhang et al., 2001). The internal structure of
81 strike-slip faults is dominated by vein arrays and hydraulic breccias. These
82 features result from intense, deep-seated, and localized hydrothermal fluid flow
83 (Cox and Munroe, 2016). Fluid flow history can be investigated in exhumed faults
84 and fractures, which provide information about deformation mechanisms, fluid-
85 rock interactions, and bulk chemical redistributions (Arancibia et al., 2014;
86 Steyrer and Sturm, 2002). Among other features, synthetic faults, antithetic faults,
87 deformation bands, joints, stylolites, veins, and breccia have been recognized in
88 strike-slip fault zones affected by hydrothermal fluids (e.g., Fossen and Rotevatn,
89 2016; Choi et al., 2016; Liao et al., 2017; Peacock et al., 2017a, 2017b; Alsop et
90 al., 2020; Ostermeijer et al., 2020). However, there is a debate about which of
91 these structures, if any, exerts a primary influence on fluid flow and the role and
92 origin of fluids in strike-slip fault zones (e.g., Gudmundsson et al., 2002;
93 Gudmundsson, 2007).

94 Several studies show that hydrothermal deposits occur in the São Francisco
95 Craton region, including those around fault zones, while the region remained
96 tectonically stable during the Brasiliano/Panafrican orogenic cycle at 740-540 Ma
97 (e.g., Almeida et al., 2000; Brito Neves et al., 2014). This study focuses on the
98 Cafarnaum fault zone, which occurs as a lateral ramp (Fig. 1A, B, C, D). However,
99 the relationship between the location and timing of hydrothermal deposit
100 formation and fault geometry and evolution remains elusive.

101 This study is a multiscale and multidisciplinary approach that uses remote
102 sensing, aeromagnetic data, field observations, petrography, and stable isotope
103 geochemistry to compare the structural evolution of the hydrothermal system in

104 the siliciclastic and carbonate host rocks along the Cafarnaum fault zone and the
105 inner basin. We present stable isotope analyses on carbonate host rocks, veins,
106 pockets, and fluid inclusions of the inner basin to reconstruct fluid-rock
107 interactions and build a model to predict the development of hydrothermal activity
108 on a regional scale, which can be used as a proxy for other basins elsewhere.
109 New stable isotope data of fluid inclusions and veins and previously published
110 data of sulfur in sulfides show that carbonate veins associated with fractures at
111 the edge of the basin record much higher temperatures than those crystallized in
112 the central part of the basin. This study also describes and discusses the
113 kinematics, morphology, and magnetic characteristics of the fault zone and the
114 formation of various types of hydrothermal dilation breccias in the damage zone.
115 Finally, a comparison of the Precambrian Cafarnaum fault system and its host
116 rocks with other faults that affect other carbonate and siliciclastic units helps
117 understand regional predictability. This study concludes that fluid flow occurs
118 mainly along extensional subsidiary faults and investigates the way they deform
119 the host rocks. The isotope data indicate that fluids are meteoric in origin and,
120 compared to the sedimentary basins, fluids that percolated the crystalline terrain
121 may have circulated into much deeper zones.

122 **2. Geological setting**

123 The study area is mainly composed of Mesoproterozoic rocks of the
124 Chapada Diamantina Group and Neoproterozoic units of the Una Group,
125 primarily the Salitre Formation (Fig. 1D, E). The groups contain distinct
126 formations and contrasting structural styles. Both major terrains are bounded by
127 a strike-slip fault that we name the Cafarnaum fault in this study. It acted as a
128 tectonic boundary between the aforementioned Mesoproterozoic and
129 Neoproterozoic units (La Bruna et al., 2021).

The Chapada Diamantina Group is 1,000 m thick and includes the Morro do Chapéu Formation, which was deposited at ~1400-900 Ma (Pedreira et al., 1975; D'Angelo et al., 2020). This unit was affected by a first contractional inversion event that is mainly marked by symmetrical, N-S-trending, open folds (Danderfer et al., 2015; D'Angelo et al., 2020). High-angle fractures strike mostly N-S, NE-SW and NW-SE, and have a high degree of symmetry with the N-S regional folds (Danderfer et al., 2015).

The Salitre Formation is ~750 m thick in the central part of the Irecê Basin (D'Angelo et al., 2020), which was deposited in a carbonate pelitic marine basin (Misi et al. 2005, 2011) at ~750 Ma (D'Angelo et al., 2020). This sequence was deposited in the Irecê Basin, an asymmetric graben with an approximately N-S-oriented axis that plunges toward the north (Lagoeiro, 1990; Kuchenbecker et al., 2011; Brito Neves et al., 2012; D'Angelo et al., 2020). The Irecê Basin was inverted in the Brasiliano orogeny, with a peak at ~600 Ma, which resulted in anomalous deformation concerning adjacent domains, with a series of south-verging fold and thrust systems (Lagoeiro, 1990; Teixeira et al., 2019; D'Angelo et al., 2020).

The carbonate units of the Irecê Basin have similar Pb-Pb isochron ages and paleomagnetic poles, which fall close to ~520 Ma. This age is consistent with the Gondwana supercontinent's apparent polar wander path and indicates that isotopic and magnetic systems reset those of the Cambrian (Trindade et al., 2004). This event was related to regional-scale fluid migration and subsequent mineralization at the end of the Brasiliano orogenic cycle (Trindade et al., 2004).

An E-W-oriented magnetic telluric section across the Irecê and Morro do Chapéu Basins reveals lithospheric resistive blocks bounded by major conductive

deep zones, which are interpreted as faults. It shows that a lithospheric conductor, interpreted as a suture zone, occurs between the Neoproterozoic Irecê Basin and the Chapada Diamantina Group (Fig. 1D). The high conductance zone is a combination of high porosity and high fluid salinity (Padilha et al., 2019).

Detailed geological mapping on both sides of the fault indicates a great number of occurrences of hydrothermal minerals associated with faults. These occurrences encompass metals such as Au, Pb-Zn, and Ba. These metals occur in sulfides associated with quartz veins in dolomite units close to the main faults. In a few cases, minerals such as barite also occur in the host carbonate rocks (Sampaio et al., 2001).

More detailed studies have also investigated hydrothermal silicification and dolomitization in a few karst systems. Several works, conducted in the São Francisco Craton, have already investigated cave geometry, stratigraphy, geochemistry, and mineralogy to indicate that fault and fracture systems were used as conduits for deep-seated fluid flow (Klimchouk et al., 2016; Cazarin et al., 2019; La Bruna et al., 2021; Pontes et al., 2021). In another case, approximately 100 km to the south of the study area, a N-S-striking, strike-slip fault in the southern part of the Irecê Basin was the pathway for fluid flow confined to the Salitre Formation during the Brasiliano orogeny. The first stage of Mg-rich fluids caused extensive dolomitization in the Salitre Formation, which was subsequently followed by Si-rich fluids that caused pervasive silicification in the host units (Bertotti et al., 2020).

3. Methods

The present study integrates (1) remote sensing and structural investigation, (2) Geophysical data and processing, (3) sampling, (4) mineralogy and petrography, (5) stable isotope analysis of veins and host rock, and (6) isotope geochemistry of fluid inclusions. We used the Shuttle Radar Topographic Mission (SRTM), ALOS-PALSAR to map regional structures, and unmanned aerial vehicle imagery for a detailed investigation of tectonic features (Fig. 2). The aeromagnetic data used to map fault segments are from the Centro Norte Bahia Project is an airborne magnetic survey carried out by Companhia Baiana de Pesquisa Mineral (CBPM) (Fig. 3). The petrography, mineralogy, isotope, and fluid inclusions are based on the analysis of six outcrops in carbonate units of the Salite Formation on both sides of the Cafarnaum fault. We present a complete description of data and methods in the supporting material section (Methods – supporting material).

4. Results

4.1 *Qualitative field fracture analysis*

Different fracture types were distinguished; joints display their peculiar plumose morphology (Pollard and Aydin, 1988), and are compart mentalized or not within single beds (Fig. 4). For this reason, they are here named stratabound (SB) and non-stratabound (NSB) fractures. Veins are also SB and NSB, but in some outcrops they are subvertical and parallel to the tilted bed layers (Fig. 4C, D and F). Clustered fracture and vein networks were in the proximity of fault zones (Fig. 5B,C, D and E). In particular, the high-resolution qualitative structural analysis shows the following fracture sets: subvertical NW-SE fractures and veins (Fig. 4G, H and Fig.5B,C, D, E, F, G and H); minor subvertical NE-SW fractures and veins (Fig. 4G and Fig.5B,C, D, E, F, G and H); minor subvertical N-S fractures

and veins (Fig.5C, D, and F); and subvertical E-W bed-parallel veins (Fig. 4C, D and F).

4.2 Macroscale geometry and kinematics of the Cafarnaum fault

The compiled structural map presents the primary structural alignments in an area of 38,000 km^2 (Figs. 2A, B, C, 3A, B). The tectonic structures were sorted into strike-slip faults, normal faults, reverse faults, and fold hinges based upon new original data interpretation and previous geological mapping (Cazarin et al., 2019; D'Angelo et al., 2019; Ennes-Silva et al., 2015; Souza et al., 2003). The satellite alignments were divided into the following three fault sets: NNE-SSW, NE-SW, and NW-SE. The NNE-SSW set is generally associated with strike-slip left-lateral faults, as already presented by D'Angelo et al. (2019) and Danderfer Filho et al. (2015). A zone of restraining bends coincides with an uplifted area (Fig. 2A). Additionally, drag folds occur on the west side of the Cafarnaum fault. The folded structures are E-W-striking thrusts of the Irecê Basin that bend where they reach the Cafarnaum fault. Bed layers associated to these thrust faults were tilted to the subvertical position (Fig. 4A). In some case, the aforementioned subvertical bed interfaces were affected by shearing as displayed by several kinematics indicators (Fig. 4B). Many mineralized portions documented as bed parallel veins occur along bed interlayers (Fig. 4C, D and F). Some of the thrust faults display drag folds as they approach the Cafarnaum fault. In contrast, the NE-SW- and E-W-oriented sets are composed of reverse faults, as shown by D'Angelo et al. (2019) and Reis et al. (2013).

The NW-SE fault set has been interpreted as composed of normal faults (D'Angelo et al., 2019). Termination zones of horsetail geometry occur at both

ends of the Cafarnaum fault (Fig. 2C). A few minor faults associated with veins and breccia bodies also occur at the central part of the fault zone, as at the MAM site (Fig. 5). These zones are marked by NW-SE-striking extensional faults located at the extensional quadrant of the main N-S-striking fault zone (La Bruna et al., 2021). There, hydrothermal deposits concentrate on a 20 km wide zone on both sides of the central fault (Fig. 2A, C). Several hydrothermal minerals (e.g., barite, galena) were documented in the Mam outcrop (Fig. 5B, C, D and E). In these sites, complex vein/fracture networks were observed. Both veins and fractures form a principal NW-SE striking set and a minor NE-SW set.

Both the NE-SW- and NW-SE-striking fault sets terminate against the NNE-SSW- to N-S-striking fault set. Eastward from the Cafarnaum fault, a larger folded zone was documented (Fig. 2B, C). Previous works have described how this sector is affected by several anticlines and synclines (Cazarin et al., 2019; D'Angelo et al., 2019; Danderfer Filho et al., 2015; Ennes-Silva et al., 2015; Souza et al., 2003). The fold hinges mainly trend along the NNE-SSW to N-S directions (Fig. 2B, C).

An area of ca. 14,000 km^2 was analyzed for structural magnetic lineament map characterization (Fig. 3A, B). The 2,818 documented lineaments were sorted into , I-order , II-order, and III order lineaments. The I-order lineaments are related to regional-scale magnetic features and are composed of a major NE-SW set and minor sets striking N-S and E-W, respectively. The II-order lineaments are characterized by a major NE-SW lineament and a minor NW-SE to WNW-ESE set associated with secondary magnetic anomalies. Both I- and II-order lineaments are crosscut by the III order lineaments.

The III order lineaments exhibit a singular magnetic pattern, distinguished by striking high-amplitude magnetic lineaments with the extension of dozens of kilometers (Figs. 3A, B). They occur isolated or comprising sets with main NW-SE and minor NE-SW orientations. Sometimes, they are stepwise segmented (en echelon) and shifted by hundreds of meters. They truncate other magnetic lineaments in high to moderate angles, indicating a more recent geological event. Due to high magnetization contrast with bedrocks, linear and extensive waveform, and sparse spatial distribution, we associate these magnetic lineaments with mafic dikes as many authors elsewhere (e.g., Schwarz et al., 1987; Demarco et al., 2020). In fact, the NNW-SSE trending Chapada Diamantina mafic dike swarm is intrusive into the Mesoproterozoic sedimentary sequences of the Espinhaço Supergroup within the Paramirim Aulacogen (Brito, 2008; Silveira et al., 2013). The magnetite-bearing dikes are fine to medium-grained diabases. Recently Pessano et al. (2021) associated NW-SE oriented magnetic anomalies in the central portion of the São Francisco Craton with Mesoproterozoic dikes of the Chapada Diamantina swarm.

4.3 - Hydrothermal vein and breccia characterization

Two main types of structures related to hydrothermal activity occur in the Cafarnaum fault zone and its surroundings. The first type is hydrothermal breccias, which mainly occur in dilational jogs. The second is calcite veins, which are widespread in the fault zone and the host rocks away from the fault. Two sites of hydrothermal breccias occur along NW-SE striking extensional faults, which we describe below. In addition, we describe four sites with calcite veins at varying distances from the Cafarnaum fault.

Hydrothermal breccias are characterized by the interaction between rocks and hydrothermal solutions and are geometrically characterized by several parameters, such as morphology, particle size distribution, fabric, and expansion radius (Jébrak, 1997). Chemical and physical mechanisms can form these breccia bodies: the first by selective dissolution and the second by the excess tension exerted, which exceeds the tensile resistance of the material, or in some combination. The analyzed bodies are classified as mosaic breccias that are formed by fluid-assisted breach (hydraulic fracturing) using the classification given by Jebrák (1984b). Carbonate clasts are present, and clasts that are larger than 2 mm range between 60-75% of clasts and 75-100% of clasts.

Hydraulic breccias are rocks composed of angular to subangular fragments of dimensions ranging from 0.4 cm to 5 cm that are cut by several generations of fractures and veins. The fragments are present throughout the breccia bodies and are derived from adjacent rocks. Generally, they are monolithologic and represented by carbonate rocks corresponding to the Salitre Formation.

Carbonates also contain calcite and quartz geodes surrounded by intense oxidation (limonitization). The interfragmentary filling is composed of iron oxide or quartz and calcite cement. The oxidized matrix is probably formed to replace rich materials in iron from the cementing fluid. Quartz is associated with calcite, galena, and malachite. There is intense veining by a network of veins with a branched structure that range from millimeters to centimeters thick and reach 30% of the total volume, and calcite veins of lesser thickness are related to quartz veins.

303 The description of carbonates can be compared to descriptions made by
304 Souza et al. (1993), such as the association of intensely closed algal laminites
305 corresponding to the Nova América inferior subunit (transgressive cycle III) at the
306 MEL site, as well as area descriptions by Misi (1975) of fine dolomites with
307 ankerite, barite and galena and light dolomites with millimeter bands, calcite
308 impregnations and microcrystals of pyrite and galena. Nevertheless, occurrences
309 only include sedimentary gaps along the Irecê Basin (Bonfim et al., 1985, and
310 Souza et al., 1993).

311 The descriptions were made under transmitted light optical microscopy of
312 the samples corresponding to MAM and MEL sites (Fig. 2A, C); the samples were
313 divided into laminated carbonates with veins, laminated carbonates with a brittle
314 aspect, and only the veins. The composition in these three divisions presents the
315 same mineralogy in carbonates and the same mineralogy in the veins,
316 differentiated by laminar and massive textural aspects in the case of carbonate
317 alteration and fragmented textural aspects.

318

319 *4.4 Mineralogy, texture, and isotope geochemistry*

320 Sites from the central part of the basin (SOR, IRE, and ACH) and the
321 eastern block (FAR) (Fig. 2C) are large carbonate pavements in which primary
322 sedimentary features are observed. Except for the FAR site, these carbonates
323 display vertical bedding and are crosscut by centimetric calcitic veins.

324 The limestones from the SOR site consist of microbial mats. The beds are
325 oriented subvertically within tight N-S-trending folds (Fig. 2C). Two types of veins
326 are observed at the SOR site. The first type of veins formed on transverse fault
327 planes, which originate in E-W-striking low-angle thrust faults, predating folding

328 to the present-day subvertical position (T16 and T19). The second type forms N-
329 S-trending veins. These veins are associated with younger N-S shortening (T24).
330 Isotope profiles across the veins reveal no significant difference in $\delta^{13}C$ and $\delta^{18}O$
331 concentration between the carbonate host rock and the transverse fault
332 carbonate filling (Fig. 6A-D).

333 The FAR site (Fig. 6E-H) consists of stromatolite bioherm colonies. Two
334 veins were analyzed. The first vein (T9) occurs in inter-stromatolite silt crosscut
335 by a sharp-edged 2.2 mm thick vein, filled with mosaic equidimensional
336 transparent calcite varying from 0.05 mm to 0.2 mm. The other vein (T10)
337 crosscuts a stromatolite unit. It has two different calcite fabrics: an
338 equidimensional mosaic with oriented sparry calcite crystals varying in size from
339 0.1 to 1 mm and a milky white area with no calcite crystals. Most calcite veins
340 from the FAR site display lower $\delta^{13}C$ and $\delta^{18}O$ values than the stromatolite host
341 rock. Exceptions are a few carbonate samples from the vein that crosscut the
342 inter-stromatolite silt (Fig. 6G-H).

343 The ACH site consists of subvertical NNW-dipping dolostones. The
344 present-day NNE-SSW burial fault carries most veins and is more prominent than
345 its conjugate NW-SE counterpart (Fig. 7A-D). Veins at the ACH site lack signs
346 of shear and are syntaxially filled with blocky crystals. In addition to veins, the
347 ACH site contains a pocket filled with crystal precipitates (T5) in which borders
348 are vein wall remnants and dissolved host rock peloids (Fig. 7B-C). Since these
349 pockets dissolve burial-related fractures and faults, they formed later than the
350 burial fault set. In general, ACH samples show a higher porosity than other sites.
351 Isotope data across these veins reveal much lower $\delta^{13}C$ and $\delta^{18}O$ values than the
352 isotope values of the host rock (Fig. 7C-D).

353 Carbonate rocks of the IRE site consist of thinly layered (0.2-20 cm) black
354 limestones with local slumps. The beds are vertically tilted and folded, with an
355 orientation of 355/86 (dip azimuth direction). Two types of veins are present (Fig.
356 97E-F): thinner (<1 cm) bedding-perpendicular and bedding-parallel pre- or
357 synfolding veins and thick veins (20 cm) filled with a mixture of calcite and barite
358 that irregularly crosscut folded bedding. They are syn- or post-folding veins.
359 Similar to the SOR site veins, IRE veins have isotope values similar to the host
360 rock (Fig. 7E-F).
361 In contrast to sites in the central part of the basin, sites at the basin edges
362 (i.e., MEL and MAM) are strongly deformed and exhibit pervasive hydrothermal
363 features and hydraulic hydrothermal breccias (Fig. 8A-C). Samples from the MEL
364 site are mostly breccias with white calcite cement. Previous studies by Misi et al.
365 (2005) argue that the Salitre Formation stratigraphy controls the Pb-Zn
366 concentrations. According to these authors, the Pb-Zn ore is associated with
367 silicified stromatolites that overlie a shallowing-upward sequence (Unit B1). The
368 MEL site is located in a flat area where sites are restricted to trenches dug by
369 mining operations. Samples may exhibit primary lamination similar to rocks of the
370 Salitre Formation. These features are obliterated by tectonic and hydrothermal
371 processes toward the center of the brecciated zone at the outcrop scale (Fig. 8A).
372 Clasts of primary carbonate rocks may also occur in the hydrothermal breccia
373 cemented by white calcite devoid of laminations (Fig. 8B). Secondary vugular-
374 type porosity that is less than 1% in the area is also observed under the
375 microscope. The limestones and breccias are crosscut by two generations of
376 veins: one measuring 4 mm thick and made of calcite and, quartz microcrystals
377 and a second measuring approximately 0.3 mm thick and made of quartz. The
378 host carbonate and the cement display quite distinct mineralogy. The primary

Salitre carbonates consist mainly of calcite, dolomite, ankerite, siderite, iron oxide, and limonite. SEM, XRD, and QUEMSCAN data indicate that the veins and hydrothermal breccias display complex mineralogy, where the main minerals are calcite, dolomite, galena, barite, quartz, sphalerite, illite, chlorite, zincite, cerussite, malachite, magnesite, apatite, and chalcedony. Barite, apatite, chlorite, and quartz are concentrated along fracture zones (Fig. 8D-G) and, in some instances, may form larger aggregates. Thin section observations indicate that tectonic and hydrothermal processes were accompanied by the formation of stylolites, dolomitization, silicification, limonitization, microfractures, folding, and minerals with wavy extinction.

Samples (Figs.8D and E) at the MEL site display different facies of carbonate breccia and isotope $\delta^{13}C$ and $\delta^{18}O$ analyses performed at specific points in the samples. While the $\delta^{13}C$ values range between 0.22‰ and -2.24‰, the $\delta^{18}O$ values vary from -6.16‰ to -12.67‰. In most instances, the primary limestone fabric was replaced by milky carbonate with large anhedral crystals. Sample in Fig. 8C displays a cyclic succession of milky calcite and iron-rich dolomite crosscut by veins containing galena. High-resolution $\delta^{13}C$ and $\delta^{18}O$ data indicate that these samples may have an area with homogenous isotope values (Fig.8D-E), as well as areas with variable isotope values.

The MAM site is also located in a flat area in which sites are restricted to trenches of the mining operation. Centimetric veins of milky quartz occur in the carbonate host unit. As at the MEL site, XRD and SEM data at the MAM site indicate galena, zincite, ankerite, dolomite, cerussite, apatite, magnesite, anglesite, chlorite, and illite. However, in contrast to the MEL site, the MAM site exhibits strong silicification that may completely obliterate the primary carbonate texture. For instance, the QUEMSCAN images exhibit carbonate breccias

405 replaced by silica in which ghost clasts can still be identified. Pores and laminated
406 illite and chlorite areas indicate that silica-rich fluids replaced mostly carbonate
407 minerals
408
409 *4.5 - Fluid inclusions*
410 Table 01 presents the H and O isotopic compositions of fluid inclusions for 10
411 samples from the ACH, IRE, and SOR sites in the Irecê Basin and at the FAR
412 site in the eastern block of the Cafarnaum fault. The supplemented materials
413 detail linearity and memory effect corrections applied to the H and O fluid isotope
414 data. Table 01 also shows the average $\delta^{18}O$ isotopic composition of the carbonate
415 associated with the fluid inclusions and the calculated temperature based on the
416 isotope fractionation between calcite and water. The calculated temperature
417 range is 40-74°C, with the highest values obtained in samples from the ACH and
418 FAR sites
419 Except for one sample from the ACH site (ACH01.3Aa T5-1, left), all samples
420 display negative δD_{SMOW} values. Fig. 9 plots the H and O isotope values with the
421 global meteoric water line (GMWL) by Rozanski et al. (1993) and shows that the
422 trending lines of samples from the ACH and FAR sites converge to a δD value of
423 approximately -45‰ and a $\delta^{18}O$ value of -6.5‰.
424
425 **5. Discussion**
426 *5.1 – Fault evolution and hydrothermal fluids*

427 Cratons are composed of thick and cool lithospheric keels with high resistivities
428 and low porosities (e.g., Ferguson et al., 2012; Selway, 2014). However, several
429 studies have increasingly indicated that cratons present low-resistivity zones in
430 the lithosphere that behave as weakness zones prone to deformation, such as

ductile shear zones and faults (e.g., Pinto et al., 2010; Thiel and Heinson, 2013; Dong et al., 2015). These shear zones/faults provide a high permeability and are pathways for deep-seated fluids to ascend through the whole lithosphere (Caine et al., 2010; Bense et al., 2013). The study of hydrothermal fluids in fault zones in cratons may explain the permeability of fault zones and host units and deep geothermal exploration constraints (Taillefer et al., 2017). The boundary between the Irecê Basin and the Chapada Diamantina Group is marked by the Cafarnaum fault (Figs. 1, 2) (La Bruna et al., 2021), which coincides with a high conductor mapped by a magnetotelluric survey (Fig.10). This zone was prone to hydrothermal activity and is consistent with high porosity-permeability, high-fluid salinity, and sulfide emplacement. In a few cases, it served as a conduit for mafic volcanism (Teixeira et al., 2017; Padilha et al. 2019).

Faults behave as high permeability conduits that facilitate fluid flow in the Earth's crust (Cox and Munroe, 2016). Deep-seated hydrothermal fluids precipitate minerals that form veins and breccias and decrease the permeability of the lithospheric fault zones (Sibson et al., 1988, 1990). The precipitation of hydrothermal minerals in fault zones and host rocks is caused by decompression and cooler conditions (Calvin et al., 2015). Therefore, based on the characteristics presented here, the Cafarnaum fault was a structure prone to hydrothermal activity. It controlled the upward hot fluid flow, indicated by the relationship between fault geometry and hydrothermal deposits (Fig.10).

. Hydrothermal fluids channelized along faults can affect thousands of square kilometers, even in nonmagmatic settings (Nabavi et al., 2020). The hydrothermal activity in faults with shallow crustal levels under fluid overpressure is controlled by the geometry of the crustal-scale fault zone (Bellot, 2008). Dilational jogs flanking continental-scale strike-slip faults, for example, are

457 locations prone to hydrothermal boiling and implosive brecciation (Sibson, 1987).
458 Active examples of hydrothermal activity in dilational jogs occur in compressional
459 settings such as New Zealand (Brathwaite et al., 1986 in 24) and the French
460 Pyrenees (Taillefer et al., 2017).

461 We interpret the N-W-striking faults that arrest against the main N-S-
462 trending Cafarnaum fault as dilational jogs that facilitate hydrothermal fluid
463 ascension and flow (Fig.10). Hydrothermal minerals are concentrated in dilational
464 jogs on both sides flanking the Cafarnaum fault, either on carbonate units in
465 the western block or mainly on siliciclastic units in the eastern block (Fig. 2). This
466 indicates that the structure, rather than the lithology, controls the fluid flow along
467 the fault.

468 Hydrothermal breccias occur in dilational jogs on both sides of the main
469 Cafarnaum fault (Fig. 2A, C). These breccias form when fluid migration becomes
470 explosive (e.g., Jébrak, 1997). Subsequent precipitation of hydrothermal minerals
471 forms breccias and heals the fault, decreasing their permeability (Katz et al.,
472 2006; Taillefer et al., 2017). Fluid flow and subsequent precipitation have been
473 interpreted with the seismic cycle and fault-valve behavior, influencing breccia
474 occurrence (Taillefer et al., 2017).

475 The results shown in this study document how strike-slip faults such as the
476 Cafarnaum fault are efficient pathways for fluids and that these fluids caused the
477 widespread silicification and the precipitation of Ca-bearing minerals. A recently
478 performed in the Morro Vermelho Karst System, located some 150km to the S of
479 the Cafarnaum fault and developed within the same carbonate succession,
480 provides more insights into the temporal succession of fluid circulation and
481 precipitation/dissolution (Bertotti et al., 2020). During the first stage, fluids flowed
482 along two main aquifers, the Chapada Diamantina quartz arenites and the

483 overlying Salitre Formation carbonates, separated by the Bebedouro Formation
484 glacial sediments aquitard. The flow was associated with pervasive dolomitization
485 of a 100s of m wide body overlying a deep-seated strike-slip fault in the
486 carbonates. With increasing displacement, the strike-slip fault grew upward (e.g.,
487 Dooley and Schreurs, 2012), thereby first affecting the Chapada Diamantina
488 aquifer and eventually reaching the Salitre carbonates. With establishing a
489 through-going fracture zone, Si-rich fluids previously confined to the Chapada
490 Diamantina aquifer invaded the Salitre aquifer, causing widespread dissolution
491 and karst formation and precipitation of Si both in the host rock as a silica-crust
492 coating the caves. We suggest that such a temporal succession could also be
493 applicable to the mineralizations of the Cafarnaum fault zone.

494

495 *5.2 – Geochemistry of hydrothermal fluids, fluid pathways and tectonics*

496 Fluid flow in the crust is a powerful mechanism to remobilize chemical
497 elements and concentrate metals of economic interest (Heinrich and Candela,
498 2014, Yardley and Bodnar, 2014).. The efficiency of heat transfer and chemical
499 remobilization depends on heat and chemical gradients, fluid-rock interactions,
500 and tectonic settings. Many studies have addressed the question of how deep
501 fluid penetrates the crust (e.g., Nesbitt and Muehlenbachs, 1989; Fricke,
502 Wickham et al., 1992; Haines, Lynch et al., 2016). Most authors agree that fluid
503 may penetrate as deep as 10 to 15 km into the crust, mainly in crystalline terrains
504 submitted to an extensional tectonic regime.

505 The isotope data presented here show that fluid sources in the central part
506 and at the Irecê Basin edges had the same origin but underwent distinct
507 pathways. The new data presented in this study allow a discussion of the source
508 of these fluids, their primary isotopic composition, their interaction with the

sedimentary rocks on both sides of the Cafarnaum fault, and how deep they may have penetrated each kind of terrain.

Different generations of carbonate veins and breccias crosscut the sedimentary rocks of the Irecê Basin. Figs. 6 and 7 show that carbonate veins from the central part of the basin do not display significant carbon and oxygen isotope differences relative to the carbonate host rock. More significant isotopic differences occur in samples from the ACH and FAR sites, where the veins present more negative isotopic values than the host rock (Fig.6).

Data in this study suggest that the $\delta^{18}O$ value of the carbonate veins may be explained by a meteoric fluid source (Fig.11), by a higher temperature of crystallization (Table 02) of these carbonates, or by the combination of both processes. The oxygen isotope fractionation between calcite and water varies from 28‰ to 7‰ in the temperature range of 25-250°C (Chacko et al. 1991; Kim, O'Neil et al., 2007; Chacko and Deines, 2008). In contrast, the low $\delta^{13}C$ values observed in the carbonate may only be explained by an external source of carbon, since the carbon isotope fractionation values between calcite and HCO_3^- and calcite and CO_2 are much less than 4‰ at temperatures below 200°C (Deines et al., 1974; Chacko et al., 1991; Chacko and Deines 2008). Samples from the MEL site, which are located at the edge of the basin, display even more negative oxygen isotope values. As shown in Fig. 11, isotope data from this site display a narrow range of $\delta^{13}C$ values and a wide range of $\delta^{18}O$ values. Compared to the veins from the central part of the Irecê Basin, the lower $\delta^{18}O$ values of their carbonates indicate interactions with more ^{18}O-depleted fluids or higher crystallization temperatures.

Fig. 11compares the isotopic composition of the carbonates studied here with previous isotope data reported for the same area. The diagram shows that

535 the data in this study have a wide range of $\delta^{18}O$ (-13.0‰ to 1.8‰) and $\delta^{13}C$ (-
536 10‰ to 10‰) values. However, most of our samples have a narrower range of
537 $\delta^{13}C$ (-5‰ to 1‰). The exceptions are samples from the IRE site that exhibit
538 higher $\delta^{13}C$ values and a few samples from the ACH, FAR, and SOR sites that
539 present $\delta^{13}C$ values below -5‰. Samples from the IRE site are associated with
540 ^{13}C-enriched carbonates from the upper section of the Irecê Basin and plotted as
541 squares in Fig. 9 . These primary high $\delta^{13}C$ carbonates have been reported in
542 both the Irecê Basin (Misi 1988, Misi and Kyle 1994, Borges, Balsamo et al. 2016,
543 Caird, Pufahl et al. 2017) and other Neoproterozoic basins (Santos, Alvarenga et
544 al. 2000). Carbonate veins with $\delta^{13}C$ values below -5‰ are probably related to
545 the same fluid that is responsible for the carbonates that formed the calcretes
546 previously described in the basin (Borges, Balsamo et al. 2016, Caird, Pufahl et
547 al. 2017). Published isotope data of these carbonates, plotted as "stars" in Fig.11,
548 also present low $\delta^{13}C$ values.

549 The source of fluids related to the carbonate veins from the central part of
550 the Irecê Basin may be further constrained by the isotopic composition of fluid
551 inclusions trapped in the carbonate veins. Based on the oxygen isotopic
552 composition of these fluid inclusions and the associated carbonate, we estimate
553 the temperature of carbonate crystallization to be between 39 and 67°C (Table
554 02). These temperature estimates were based on Kim and O'Neil (1997) oxygen
555 isotope fractionation equation between calcite and water. Since calcite and fluid-
556 inclusions may be affected by post-entrapment isotope exchange during
557 exhumation (Nooitgedacht et al., 2021), these results should indicate minimum
558 temperature conditions. Assuming an average thermal gradient of 30 C/km, these
559 fluids circulated at depths reaching 1000 m within the crust. Fig. 9 displays the
560 mean global meteoric water line by Rozanski et al. (1993) and the hydrogen and

561 oxygen isotope values of these fluid inclusions. It also shows trending lines for
562 fluid inclusions from the ACH and FAR sites, indicating that they converge to a
563 δD value near -45‰ and a $\delta^{18}O$ value near -6.5‰ along the mean meteoric water
564 line (Fig. 9). We argue that these isotopic values represent the local meteoric
565 water, which upon interaction with the host rock changed its isotopic composition
566 along the mixing lines. A similar process has been described in active
567 hydrothermal systems (Criss and Taylor Jr, 1986), in which there is also a more
568 extensive range of $\delta^{18}O$ values compared to δD values.

569 The isotopic variation observed in Fig. 11 may be explained by different
570 geological scenarios. Arrows I and II represent veins formed by mixing meteoric
571 fluids and carbonate host rocks of the inner part of the basin at low-temperature
572 conditions (between 30 and 40°C). Arrow I indicates mixing between these fluids
573 and carbonates from the lower section. In contrast, arrow II represents the mixing
574 between these fluids and the ^{13}C-enriched carbonates from the upper section.
575 Arrow III represents carbonates formed by the same fluids as those of the
576 calcretes, which have more negative $\delta^{13}C$ values. Samples from the MEL site,
577 represented by arrow IV, fall within the same range of $\delta^{13}C$ values for most
578 samples from the central part of the basin. However, they also have more
579 negative $\delta^{18}O$ values, indicating that isotope exchange between the meteoric
580 fluids and carbonates alone may not be reconciled with the observed data. We
581 argue that carbonates from the MEL site crystallized from the same meteoric fluid
582 but at higher temperatures. These fluids percolated through conduits that allowed
583 them to reach deeper parts of the crust and return to shallow crustal levels without
584 losing much heat. Compared to thrust systems alone, thrust followed by strike-
585 slip and extensional faulting may provide deep fluid conduits. Based on hydrogen
586 isotopes, Nesbitt and Muehlenbachs (1989) concluded that the tectonic regime

might drastically control the depth of fluid interaction in the crust. This interpretation also agrees with previous studies based on fluid inclusions and sulfur isotope geothermometry performed in the MEL site area (Misi and Kyle 1994, Misi, Iyer et al. 1999, Misi, Iyer et al. 2005), Fluid-rock interactions may also explain the presence of base metals in these high-temperature veins, suggesting that these chemical elements were scavenged from deeper crustal levels.

The role of deep crustal fluids at the MEL and MAM sites is further suggested by the petrographic and mineralogical features observed at these sites (Fig. 8). In addition to the high concentration of base metals (e.g., Pb, Zn, Fe), these sites display a pervasive replacement of the primary carbonates by silica. Silicification events are recognized as a diagenetic process in which Si-rich fluids affect a host rock, modifying its texture and mineralogy (Menezes et al., 2019). For example, Haldar and Tisljer (2014) documented a silicification process where opal/chalcedony/low-temperature quartz replaces calcite/aragonite/dolomite. The percolation of meteoric fluids at the deep crustal level provided the required conditions to mobilize silica at the MEL and MAM sites.

Deep meteoric fluid circulation along the Carfarnaun fault is comparable to other worldwide geological examples in which surface waters penetrate along tectonict structures. For instance, based on the Friedman and O'Neil (1977) isotope fractionation diagram, Mozafari et al. (2015) reconstructed the composition of the parent fluids that were in equilibrium with the vein infill in the Jabal Qusaybah Anticline (Adam Foothills, North Oman). The authors discussed a paleofluid evolutionary model related to the deformation front of the foreland fold and thrust belt. The strike-slip tectonic regime introduces a different type of fluid flow linked to the fault zone. The shifts in the stable isotope values forming

different fields with comparable values (Fig. 12) possibly originate from different phases of strike-slip movement. A similar spread in the fluid inclusion isotope ratios was discussed by de Graaf et al. (2020) after analyzing the wide variety of vein-type mineralization caused by deep-seated brines in the Hartz Mountains, Germany. Other studies examined the complex recrystallization processes along dolomitization fronts causing dissolution of the host limestones and precipitation of dolomite crystal structures depending on the porosity-permeability properties of the sediments present in the fault systems (Koeshidayatullah et al., 2020).

Similar to the Cafarnaun fault, the interplay between tectonics and fluid circulation has played a major role in the evolution of the inner Northern Apennines. As shown by Brogi et al. (2020), active transfer zones associated with an extensional tectonism control the deposition of travertine deposits by enhancing fluid circulation. Other studies in the same area have shown that these trending faults have also controlled the development of magmatic activities (Brogi et al., 2021) and Hg-Sb ore deposits (Brogi et al., 2011), further suggesting that these structures may connect different geological systems and play a major role in the remobilization of chemical constituents. They also indicate that competition between crustal stretching and surface uplift continuously switches the local intermediate stress axis, thus promoting quick changes in the direction of the maximum permeability (Liotta and Brogi, 2020). These changes further promote lateral and vertical migration of fluids within the system.

6. Conclusion

This study in the São Francisco Craton focuses on the hydrothermal activity in the Cafarnaum fault and its host rock and yields the following

conclusions. The São Francisco Craton is a cold and thick block preserved from deformation in the Brasiliano orogeny (740-580 Ma). However, a few tectono-thermal events affected the Craton along its boundary in Neoproterozoic times. One of these events was repeated hydrothermal activity along the Cafarnaum fault, a N-S-striking, 170 km long, strike-slip fault that juxtaposes Neoproterozoic carbonate units and Mesoproterozoic siliciclastic-carbonate units in the northern part of the Craton.

Hydrothermal boiling and implosive brecciation occurred along the fault. Decompression and cooler conditions induced precipitation of hydrothermal minerals in N-W-striking dilational jogs, mainly flanking the northern and southern fault terminations. The hydrothermal fluid structures are composed of hydrothermal breccias close to the main fault zones and along dilational jogs. In addition, calcite veins in the host units away from the fault are also part of the hydrothermal system. Therefore, the geometry of faults at shallow crustal levels influences the location of hydrothermal deposits.

Based on isotopic geochemistry, we show that meteoric water was the main fluid source that percolated the sedimentary rocks of the Irecê Basin and the Cafarnaum fault zone. Fluid inclusions in carbonate veins from the central part of the basin indicate a meteoric fluid with a δD value near -45‰ and a $\delta^{18}O$ value near -6.5‰. Temperature estimates based on the oxygen isotopic fractionation between the carbonate veins from the central part of the basin and the trapped fluid inclusions indicate temperatures ranging between 40 and 70°C. These temperature conditions agree with the lower $\delta^{18}O$ values of veins compared to the carbonate host rock. A similar $\delta^{18}O$ fluid value (-6.5‰) is obtained based on the interaction between these fluids and carbonates from the lower and upper parts of the succession.

In contrast, carbonates at the front edges of the basin associated with the Cafarnaum fault exhibit much lower $\delta^{18}O$ values, indicating higher crystallization temperatures. These carbonates are also associated with base metals and silica-rich fluids, suggesting that the fault behaved as a conduit for deeper fluid circulation in the basement. The mineral paragenesis (e.g., galena, sphalerite, barite, chlorite, illite, and quartz) and brecciated features associated with the veins and fault support this interpretation.

Acknowledgements

We thank Precambrian Research editor Victoria Pease and two anonymous reviewers for the positive criticism that greatly improved the study. This work is part of the first author PhD research work. This work was partially sponsored by Petrobras/UnB/UFRN (CristalDOM Project, coordinated by FHB – UFRN and CLC – Petrobras). We thank the Brazilian Agency of Oil, Gas, and Biofuels (Agência Nacional do Petróleo, Gas e Biocombustíveis, ANP).

References

Alsop, G.I., Weinberger, R., Marco, S., Levi, T., 2020. Bed-parallel slip: Identifying missing displacement in mass transport deposits. J. Struct. Geol. 131. https://doi.org/10.1016/j.jsg.2019.103952

Arancibia, G., Fujita, K., Hoshino, K., Mitchell, T.M., Cembrano, J., Gomila, R., Morata, D., Faulkner, D.R., Rempe, M., 2014. Hydrothermal alteration in an exhumed crustal fault zone: Testing geochemical mobility in the Caleta Coloso Fault, Atacama Fault System, Northern Chile. Tectonophysics 623, 147–168. https://doi.org/10.1016/j.tecto.2014.03.024

Bellot, J.P., 2008. Hydrothermal fluids assisted crustal-scale strike-slip on the Argentat fault zone. Tectonophysics 450, 21–33. https://doi.org/10.1016/j.tecto.2007.12.009

Bense, V.F., Gleeson, T., Loveless, S.E., Bour, O., Scibek, J., 2013. Fault zone hydrogeology. Earth-Science Rev. 127, 171–192. https://doi.org/10.1016/j.earscirev.2013.09.008

BjØrlykke, K., Egeberg, P.K., 1993. Quartz cementation in sedimentary basins. Am. Assoc. Pet. Geol. Bull. 77, 1538–1548. https://doi.org/10.1306/bdff8ee8-1718-11d7-8645000102c1865d

Brito, D.C., 2008. Geologia, Petrografia e Litogeoquímica dos Diques Máficos que ocorrem na porção sudeste da Chapada Diamantina, Bahia, Brasil. Master Degree thesis, Instituto de Geociências, Universidade Federal da Bahia, Brazil, 107p.

Brito Neves, B.B., Fuck, R.A., Pimentel, M.M., 2014. The Brasiliano collage in South America: A review. Brazilian J. Geol. https://doi.org/10.5327/Z2317-4889201400030010

Brito Neves, B.B., Dos Santos, R.A., Da Cruz Campanha, G.A., 2012. A discordância angular e erosiva entre os grupos Chapada Diamantina e Bambuí (Una) na folha Mirangaba-Bahia. Geol. USP - Ser. Cient. 12, 99–114. https://doi.org/10.5327/Z1519-874X2012000200007

Brogi A., Caggianelli A., Liotta D., Zucchi M., Spina A., Capezzuoli E., Casini A. and Buracchi E. (2021) The Gavorrano Monzogranite (Northern Apennines): An Updated Review of Host Rock Protoliths, Thermal Metamorphism and Tectonic Setting. Geosciences 11, 124.

Brogi A., Fabbrini L. and Liotta D. (2011) Sb–Hg ore deposit distribution controlled by brittle structures: The case of the Selvena mining district (Monte Amiata, Tuscany, Italy). Ore Geology Reviews 41, 35–48.

Brogi A., Liotta D., Capezzuoli E., Matera P. F., Kele S., Soligo M., Tuccimei P., Ruggieri G., Yu T.-L., Shen C.-C. and Huntington K. W. (2020) Travertine deposits constraining transfer zone neotectonics in geothermal areas: An example from the inner Northern Apennines (Bagno Vignoni-Val d'Orcia area, Italy). Geothermics 85, 101763.

Byerlee, J., 1990. Friction, overpressure and fault normal compression. Geophys. Res. Lett. 17, 2109–2112. https://doi.org/10.1029/GL017i012p0210Caine, J.S., Bruhn, R.L., Forster, C.B., 2010. Internal structure, fault rocks, and inferences regarding deformation, fluid flow, and mineralization in the seismogenic Stillwater normal fault, Dixie Valley, Nevada. J. Struct. Geol. 32, 1576–1589. https://doi.org/10.1016/j.jsg.2010.03.004

Calvin, W.M., Littlefield, E.F., Kratt, C., 2015. Remote sensing of geothermal-related minerals for resource exploration in Nevada. Geothermics 53, 517–526. https://doi.org/10.1016/j.geothermics.2014.09.002

Choi, J.H., Edwards, P., Ko, K., Kim, Y.S., 2016. Definition and classification of fault damage zones: A review and a new methodological approach. Earth-Science Rev. https://doi.org/10.1016/j.earscirev.2015.11.006

Choi, J.H., Edwards, P., Ko, K., Kim, Y.S., 2016. Definition and classification of fault damage zones: A review and a new methodological approach. Earth-Science Rev. https://doi.org/10.1016/j.earscirev.2015.11.006

Danderfer Filho, A., Lana, C.C., Nalini Júnior, H.A., Costa, A.F.O., 2015. Constraints on the Statherian evolution of the intraplate rifting in a Paleo-Mesoproterozoic paleocontinent: New stratigraphic and geochronology record from the eastern São Francisco craton. Gondwana Res. 28, 668–688. https://doi.org/10.1016/j.gr.2014.06.012

D'Angelo, T., Barbosa, M.S.C., Danderfer Filho, A., 2019. Basement controls on cover deformation in eastern Chapada Diamantina, northern São Francisco Craton, Brazil: Insights from potential field data. Tectonophysics 772. https://doi.org/10.1016/j.tecto.2019.228231

De Graaf, S., Lüders, V., Banks, D.A., Sośnicka, M., Reijmer, J.J.G., Kaden, H. and Vonhof, H.B. (2020) Fluid evolution and ore deposition in the Harz Mountains revisited: isotope and crush-leach analyses of fluid inclusions. Mineralium Deposita, 55, 47-62. https://doi.org/10.1007/s00126-019-00880-w

Demarco, P.N., Masquelin, H., Prezzi, C., Aïfa, T., Muzio, R., Loureiro, J., Peel, E., Campal, N., Sánchez Bettucci, L., 2020. Aeromagnetic patterns in Southern Uruguay: Precambrian-Mesozoic dyke swarms and Mesozoic rifting structural and tectonic evolution. Tectonophysics 789. https://doi.org/10.1016/j.tecto.2020.228373

Dong, Z., Tang, J., Unsworth, M., Chen, X., 2015. Electrical resistivity structure of the upper mantle beneath Northeastern China: Implications for rheology and the mechanism of craton destruction. J. Asian Earth Sci. 100, 115–131. https://doi.org/10.1016/j.jseaes.2015.01.008

Dooley, T. P., and G. Schreurs, 2012, Analogue modelling of intraplate strike-slip tectonics: A review and new experimental results: Tectonophysics 574–575, 1–71, doi: 10.1016/j.tecto.2012.05.030.

Evans, J.P., Chester, F.M., 1995. Fluid–rock interaction and weakening of faults of the San Andreas system: inferences from San Gabriel fault-rock geochemistry and microstructures. Journal of Geophysical Research. 100,13007–13020.

Ferguson, I.J., Jones, A.G., Chave, A.D., 2012. Case histories and geological applications, in: Chave, A.D., Jones, A.G. (Eds.), The Magnetotelluric Method: Theory and Practice. Cambridge University Press, New York, pp. 480–544. https://doi.org/10.1017/CBO9781139020138.012.

Fossen, H., Rotevatn, A., 2016. Fault linkage and relay structures in extensional settings-A review. Earth-Science Rev. https://doi.org/10.1016/j.earscirev.2015.11.014

Friedman, I., O'Neil, J.R., 1977. Compilation of stable isotope fractionation factors of geochemical interest: U.S. Geological Survey, Bulletin 440, 1–12. https://doi.org/10.3133/pp440KK

Gudmundsson, A., Fjeldskaar, I., Brenner, S.L., 2002. Propagation pathways and fluid transport of hydrofractures in jointed and layered rocks in geothermal fields. J. Volcanol. Geotherm. Res. 116, 257–278. https://doi.org/10.1016/S0377-0273(02)00225-1

Gudmundsson, A., 2007. Infrastructure and evolution of ocean-ridge discontinuities in Iceland. J. Geodyn. 43, 6–29. https://doi.org/10.1016/j.jog.2006.09.002

Gudmundsson, A., 2001. Fluid overpressure and flow in fault zones: Field measurements and models. Tectonophysics 336. https://doi.org/10.1016/S0040-1951(01)00101-9

Haldar, S.K., Tišljar, J., 2014. Introduction to Mineralogy and Petrology, Introduction to Mineralogy and Petrology. Elsevier Inc. https://doi.org/10.1016/C2012-0-03337-6

Haneberg, W.C., Mozley, P.S., Moore, J.C., Goodwin, L.B., 1999. Faults and Subsurface Fluid Flow in the Shallow Crust. Geophys. Monogr. Ser. 113, 222.

Hardebeck, J.L., Hauksson, E., 1999. Role of Fluids in Faulting Inferred from Stress Field Signatures. Science. 285, 236–239. https://doi.org/10.1126/science.285.5425.236.

Hausegger, S., Kurz, W., Rabitsch, R., Kiechl, E., Brosch, F.J., 2010. Analysis of the internal structure of a carbonate damage zone: Implications for the mechanisms of fault breccia formation and fluid flow. J. Struct. Geol. 32, 1349–1362. https://doi.org/10.1016/j.jsg.2009.04.014

Jébrak, M., 1997. Hydrothermal breccias in vein-type ore deposits: A review of mechanisms, morphology and size distribution. Ore Geol. Rev. 12, 111–134. https://doi.org/10.1016/S0169-1368(97)00009-7

Katz, D.A., Eberli, G.P., Swart, P.K., Smith, L.B., 2006. Tectonic-hydrothermal brecciation associated with calcite precipitation and permeability destruction in Mississippian carbonate reservoirs, Montana and Wyoming. Am. Assoc. Pet. Geol. Bull. 90, 1803–1841. https://doi.org/10.1306/03200605072

Koeshidayatullah, A., Corlett, H., Stacey, J., Swart, P.K., Boyce, A. and Hollis, C. (2020) Origin and evolution of fault-controlled hydrothermal dolomitization fronts: A new insight. Earth and Planetary Science Letters, 541, 116291. https://doi.org/10.1016/j.epsl.2020.116291

Kuchenbecker, M., Reis, H.L.S., Fragoso, D.G.C., 2011. Caracterização Estrutural e Considerações sobre a evolução tectônica da Formação Salitre na porção central da Bacia de Irecê, norte do Cráton do São Francisco (BA). Geonomos. 19, 42–49. https://doi.org/10.18285/geonomos.v19i2.40.

La Bruna, V., Lamarche, J., Agosta, F., Rustichelli, A., Giuffrida, A., Salardon, R., Marié, L., 2020. Structural diagenesis of shallow platform carbonates: Role of early embrittlement on fracture setting and distribution, case study of Monte Alpi (Southern Apennines, Italy). J. Struct. Geol. 131. https://doi.org/10.1016/j.jsg.2019.103940

La Bruna, V., Bezerra, F. H., Souza, V. H., Maia, R. P., Auler, A. S., Araujo, R. E., Cazarin, C. L., Rodrigues, M. A. F., Vieira L. C., Sousa, M. O. (2021). High-permeability zones in folded and faulted silicified carbonate rocks–Implications for karstified carbonate reservoirs. Marine and Petroleum Geology 128, 105046.

828 Lagoeiro, L.E., 1990. Estudo Da Deformação Nas Sequências Carbonáticas Do
829 Grupo Una Na Região De Irecê, BA. Departamento de Geologia,
830 Universidade Federal de Ouro Preto, Ouro Preto, MSc, thesis 105 p.

831 Liao, Z., Liu, H., Jiang, Z., Marfurt, K.J., Reches, Z., 2017. Fault damage zone at
832 subsurface: A case study using 3D seismic attributes and a clay model
833 analog for the Anadarko Basin, Oklahoma. Interpretation 5, T143–T150.
834 https://doi.org/10.1190/INT-2016-0033.1

835 Liotta D. and Brogi A. (2020) Pliocene-Quaternary fault kinematics in the
836 Larderello geothermal area (Italy): Insights for the interpretation of the
837 present stress field. Geothermics 83, 101714.

838 Mapa Geológico do Estado da Bahia-CBPM/CPRM, 2003. Levantamento
839 Aerogeofísico da Área do Centro Norte Bahia-CBPM, 2011/12.

840 Misi, A., Iyer, S.S.S., Coelho, C.E.S., Tassinari, C.C.G., Franca-Rocha, W.J.S.,
841 de Abreu Cunha, I., Rocha Gomes, A.S., de Oliveira, T.F., Teixeira, J.B.G.,
842 Filho, V.M.C., 2005. Sediment hosted lead-zinc deposits of the
843 Neoproterozoic Bambuí Group and correlative sequences, São Francisco
844 Craton, Brazil: A review and a possible metallogenic evolution model. Ore
845 Geol. Rev. 26, 263–304. https://doi.org/10.1016/j.oregeorev.2004.12.004

846 Misi, A., Kaufman, A.J., Azmy, K., Dardenne, M.A., Sial, A.N., de Oliveira, T.F.,
847 2011. Neoproterozoic successions of the São Francisco Craton, Brazil: The
848 Bambuí, Una, Vazante and Vaza Barris/Miaba groups and their glaciogenic
849 deposits. Geol. Soc. Mem. 36, 509–522. https://doi.org/10.1144/M36.48

850 Mozafari, M., Swennen, R., Balsamo, F., Clemenzi, L., Storti, F., El Desouky, H.,
851 Vanhaecke, F., Tueckmantel, C., Solum, J. and Taberner, C., 2015.
852 Paleofluid Evolution In Fault-Damage Zones: Evidence From Fault-Fold
853 Interaction Events In the Jabal Qusaybah Anticline (Adam Foothills, North
854 Oman). Journal of Sedimentary Research 85, 1525-1551.
855 https://doi.org/10.2110/jsr.2015.95
856 Nabavi, S.T., Alavi, S.A., Wibberley, C.A.J., Jahangiri, M., 2020. Normal fault
857 networks and their spatial relationships in Plio-Quaternary sedimentary
858 series: A case study in the Zanjan Depression, NW Iran. J. Struct. Geol. 136.
859 https://doi.org/10.1016/j.jsg.2020.104072

860 Ngwenya, B.T., Elphick, S.C., Main, I.G., Shimmield, G.B., 2000. Experimental
861 constraints on the diagenetic self-sealing capacity of faults in high porosity
862 rocks. Earth Planet. Sci. Lett. 183, 187–199. https://doi.org/10.1016/S0012-
863 821X(00)00261-2

864 Nooitgedacht, C.W., H.J.L. van der Lubbe, S. de Graaf, M. Ziegler, P.T.
865 Staudigel, and J.J.G. Reijmer., 2021.Restricted Internal Oxygen Isotope
866 Exchange in Calcite Veins: Constraints from Fluid Inclusion and Clumped
867 Isotope-Derived Temperatures. Geochimica et Cosmochimica Acta. 297,
868 24–39. https://doi.org/10.1016/j.gca.2020.12.008.Ostermeijer, G.A.,
869 Mitchell, T.M., Aben, F.M., Dorsey, M.T., Browning, J., Rockwell, T.K.,
870 Fletcher, J.M., Ostermeijer, F., 2020. Damage zone heterogeneity on
871 seismogenic faults in crystalline rock; a field study of the Borrego Fault, Baja
872 California. J. Struct. Geol. 137. https://doi.org/10.1016/j.jsg.2020.104016.

Padilha, A.L., Vitorello, Í., de Pádua, M.B., Fuck, R.A., 2019. Magnetotelluric images of Paleoproterozoic accretion and Mesoproterozoic to Neoproterozoic reworking processes in the northern São Francisco Craton, central-eastern Brazil. Precambrian Res. 333. https://doi.org/10.1016/j.precamres.2019.105416

Peacock, D.C.P., Nixon, C.W., Rotevatn, A., Sanderson, D.J., Zuluaga, L.F., 2017a. Interacting faults. J. Struct. Geol. 97, 1–22. https://doi.org/10.1016/j.jsg.2017.02.008

Peacock, D.C.P., Dimmen, V., Rotevatn, A., Sanderson, D.J., 2017a. A broader classification of damage zones. J. Struct. Geol. 102, 179–192. https://doi.org/10.1016/j.jsg.2017.08.004

Peacock, D.C.P., Dimmen, V., Rotevatn, A., Sanderson, D.J., 2017b. A broader classification of damage zones. J. Struct. Geol. 102, 179–192. https://doi.org/10.1016/j.jsg.2017.08.004

Pedreira, A.J., Arcanjo, J.B., Oliveira, J.E., Silva, B.C.E., 1975. Projeto Bahia: Geologia Da Chapada Diamantina (Relatório Final). DNPM/CPRM, Salvador, Texto e Mapas. 182p.

Pessano, P.C., Ganade, C.E., Tupinambá, M., Teixeira, W., 2020. Updated map of the mafic dike swarms of Brazil based on airborne geophysical data. J. South Am. Earth Sci. 66. https://doi.org/10.1016/j.jsames.2020.103076

Pinto, L.G.R., de Pádua, M.B., Ussami, N., Vitorello, I., Padilha, A.L., Braitenberg, C., 2010. Magnetotelluric deep soundings, gravity and geoid in the south São Francisco craton: Geophysical indicators of cratonic lithosphere rejuvenation and crustal underplating. Earth Planet. Sci. Lett. 297, 423–434. https://doi.org/10.1016/j.epsl.2010.06.044

Pollard, D. D., Aydin, A. (1988). Progress in understanding jointing over the past century. Geological Society of America Bulletin *100*(8), 1181-1204.

Pontes, C. C., Bezerra, F. H., Bertotti, G., La Bruna, V., Audra, P., De Waele, J.,Auler, A. S., Balsamo, F., De Hoop, S.,Pisani, L. (2021). Flow pathways in multiple-direction fold hinges: Implications for fractured and karstified carbonate reservoirs. Journal of Structural Geology 146, 104324.Rawling, G.C., Goodwin, L.B., Wilson, J.L., 2001. Internal architecture, permeability structure, and hydrologic significance of contrasting fault-zone types. Geology 29, 43–46. https://doi.org/10.1130/0091-7613(2001)029<0043:IAPSAH>2.0.CO;2

Rice, J.R., 1992. Fault Stress States, Pore Pressure Distributions, and the Weakness of the San Andreas Fault. Int. Geophys. 51, 475–503. https://doi.org/10.1016/S0074-6142(08)62835-1

Rozanski, K., Araguás-Araguás, L., & Gonfiantini, R., 1993. Isotopic patterns in modern global precipitation. Reference to a chapter in an edited book: P. K. Swart, K. C. Lohmann, J. McKenzie, & S. Savin, Climate change in continental climate records, American physical union,78, pp. 1-36.

Sampaio A.R., Santos R.A., Rocha A.J.D., Guimarães J.T., 2001. Programa Levantamentos Geológicos Básicos do Brasil - PLGB. Jacobina, Folha

SC.24-Y-C, estado da Bahia. Escala 1:250.000. Brasília, CPRM/DIEDIG/DEPAT., p. 31.

Schwarz, E.J., Hood, P.J. and Teskey, D.J., 1987. Magnetic expression of Canadian diabase dykes and downward modelling. Reference to a chapter in an edited book: Halls, H.C. and Fahrig, W.F. (Eds.), Mafic Dyke Swarms. Geological Association of Canada, Special Paper,34, pp. 153–162.

Selway, K., 2014. On the Causes of Electrical Conductivity Anomalies in Tectonically Stable Lithosphere. Surv. Geophys. 35, 219–257. https://doi.org/10.1007/s10712-013-9235-1

Sibson, R. H., 1990. Faulting and fluid flow, in B. E. Nesbitt, ed., Short course on fluids in tectonically active regimes of the continental crust: Mineralogical Association of Canada Short Course Handbook, 18, pp. 93–131.

Sibson, R.H., 1987. Earthquake rupturing as a mineralizing agent in hydrothermal systems. Geology 15, 701–704. https://doi.org/10.1130/0091-7613(1987)15<701:ERAAMA>2.0.CO;2

Sibson, R.H., Robert, F., Poulsen, K.H., 1988. High-angle reverse faults, fluid-pressure cycling, and mesothermal gold-quartz deposits. Geology 16, 551–555. https://doi.org/10.1130/0091-7613(1988)016<0551:HARFFP>2.3.CO;2

Silveira, E.M., Söderlund, U., Oliveira, E.P., Ernst, R.E., Leal, A.B.M., 2013. First precise U-Pb baddeleyite ages of 1500Ma mafic dykes from the São Francisco Craton, Brazil, and tectonic implications. Lithos 174, 144–156. https://doi.org/10.1016/j.lithos.2012.06.004

Sleep, N.H., Blanpied, M.L., 1992. Creep, compaction and the weak rheology of major faults. Nature 359, 687–692. https://doi.org/10.1038/359687a0

Smeraglia, L., Giuffrida, A., Grimaldi, S., Pullen, A., La Bruna, V., Billi, A., Agosta, F., 2021. Fault-controlled upwelling of low-T hydrothermal fluids tracked by travertines in a fold-and-thrust belt, Monte Alpi, southern apennines, Italy. J. Struct. Geol. 144. https://doi.org/10.1016/j.jsg.2020.104276

Steyrer, H.P., Sturm, R., 2002. Stability of zircon in a low-grade ultramylonite and its utility for chemical mass balancing: The shear zone at Miéville, Switzerland. Chem. Geol. 187, 1–19. https://doi.org/10.1016/S0009-2541(02)00010-4

Souza, J. D. D., Melo, R. C. D., & Kozin, M., 2003. Mapa geológico do Estado da Bahia. Escala 1 : 1.000.000. CPRM/CBPM.

Taillefer, A., Soliva, R., Guillou-Frottier, L., Goff, E. Le, Martin, G., Seranne, M., 2017. Fault-related controls on upward hydrothermal flow: An integrated geological study of the têt fault system, Eastern Pyrénées (France). Geofluids 2017. https://doi.org/10.1155/2017/8190109

Teixeira, J.B.G., Misi, A., Da Silva, M.D.G., De Brito, R.S.C., 2019. Reconstruction of precambrian terranes of northeastern Brazil along cambrian strike-slip faults: A new model of geodynamic evolution and gold metallogeny in the State of Bahia. Brazilian J. Geol. 49. https://doi.org/10.1590/2317-4889201920190009

960 Teixeira, W., Oliveira, E.P., Marques, L.S., 2017. Nature and Evolution of the
961 Archean Crust of the São Francisco Craton, in: Heilbron, M., Cordani, U.G.,
962 Alkmim, F.F. (Eds.), São Francisco Craton, Eastern Brazil: Tectonic
963 Genealogy of a Miniature Continent. Springer, Cham, pp. 29–56.doi:
964 10.1007/978-3-319-01715-0_3.

965 Thiel, S., Heinson, G., 2013. Electrical conductors in Archean mantle-Result of
966 plume interaction? Geophys. Res. Lett. 40, 2947–2952.
967 https://doi.org/10.1002/grl.50486

968 Wibberley, C.A.J., Shipton, Z.K., 2010. Fault zones: A complex issue. J. Struct.
969 Geol. https://doi.org/10.1016/j.jsg.2010.10.006

970 Yilmaz, T.I., Prosser, G., Liotta, D., Kruhl, J.H., Gilg, H.A., 2014. Repeated
971 hydrothermal quartz crystallization and cataclasis in the Bavarian Pfahl
972 shear zone (Germany). J. Struct. Geol. 68, 158–174.
973 https://doi.org/10.1016/j.jsg.2014.09.004

974 Zhang, S., Tullis, T.E., Scruggs, V.J., 2001. Implications of permeability and its
975 anisotropy in a mica gouge for pore pressures in fault zones. Tectonophysics
976 335, 37–50. https://doi.org/10.1016/S0040-1951(01)00044-0.

977

978

Figure 1

Click here to access/download;Figure;Fig.1.jpg

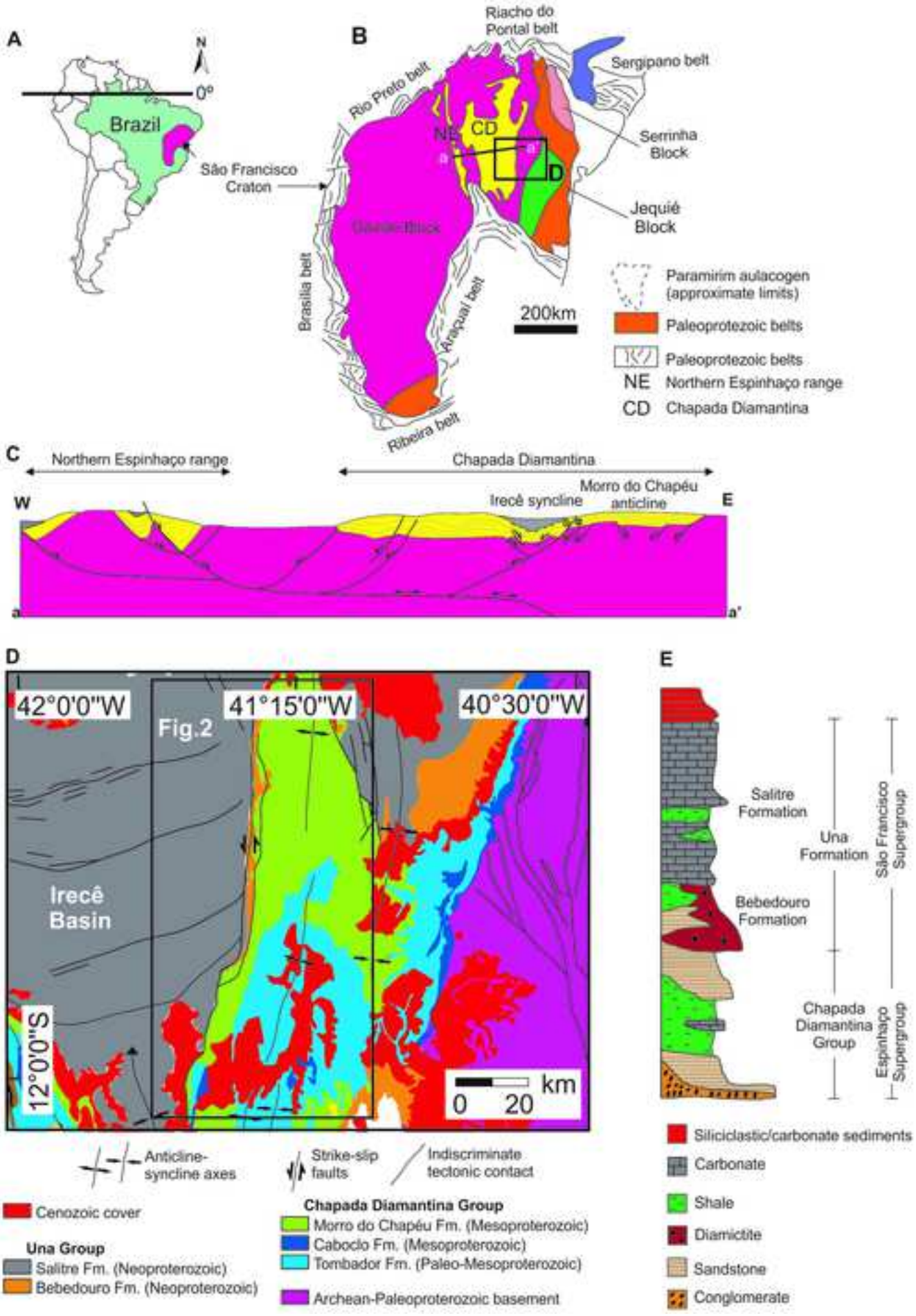

Figure 2

Click here to access/download;Figure;Fig.2.jpg

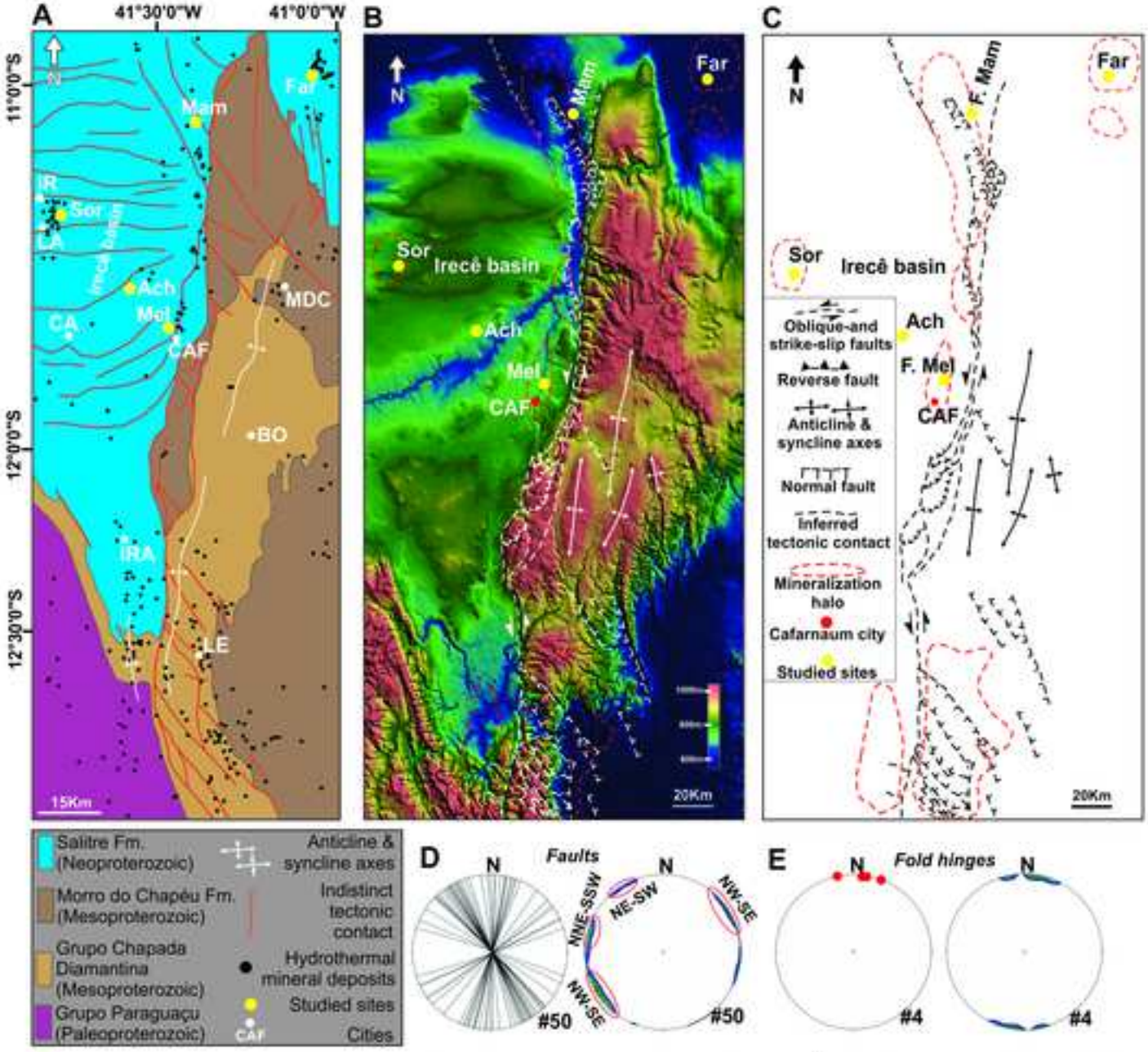

Figure 2. (A) Simplified geological map modified after *Levantamento Aerogeofisico da Área de Centro Norte Bahia - CBPM, 2011/12 Geologia - Mapa Geológico do Estado da Bahia - CBPM/CPRM, 2003.* (B) Structural framework of the study area superposed on ALOS PALSAR imagery. Dashed lines represent the inferred faults. Continuous white lines represent both anticline and syncline axes. (C) Line drawing of the structural framework presented in B. (D) Lower hemisphere equal-area projections of great circles representing the attitude of the documented faults and equal-area projection/density contour plots of the poles of the measured faults. (E) Lower hemisphere equal-area projections of fold hinges and relative density contour plots. (the map location can be found in Fig. Geological map).

Figure 3

Click here to access/download;Figure;Fig.3.jpg

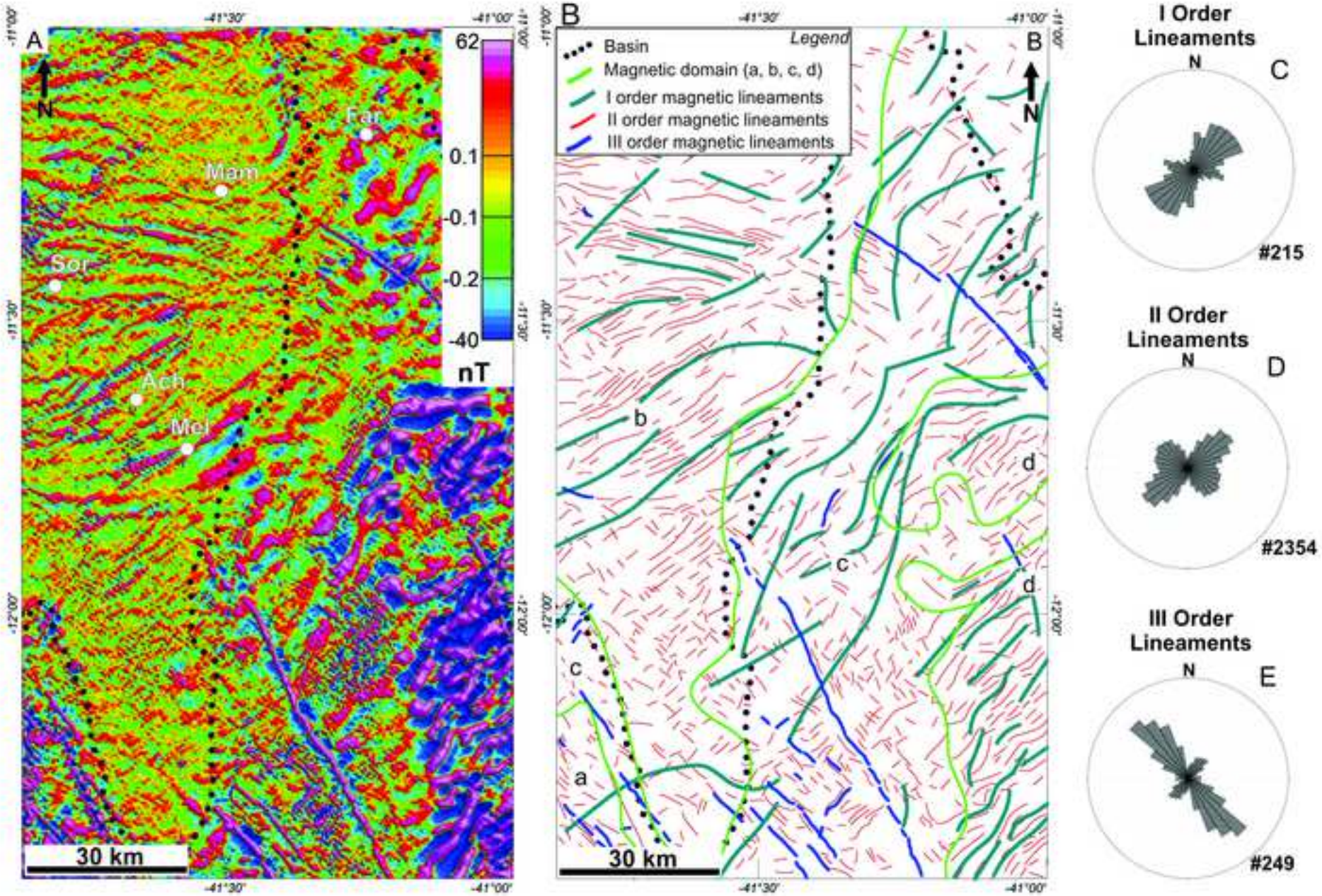

Figure 3. Behavior of magnetic lineaments in the study area: (A) Map of first derivate. (B) Lineaments Line drawing of the map presented in A. (C-D-E) Rose diagram representing the attitude of the documented first, second and third order lineaments.

Figure 4

Click here to access/download;Figure;Fig.4.jpg

Figure 4. (A) Outcrop view of subvertical bed layers in the Achado outcrop; (B) Close up view of a bed parallel slip surface. Kinematic indicators, such as striae are visible along the slip surface. (C) Close up view of a large bed parallel vein and bed perpendicular fractures; (D) Close up view of bed parallel veins and bed perpendicular fractures and veins. (E) Rose diagramm of the documented fractures in the Ach outcrop. (F) Lower hemisphere equal area projection of veins measured in the Ach outcrop. (G) and (H) Rose diagramm of the documented fractures and veins in the Far and Sor outcrops. See Fig. 2 for outcrops location.

Figure 5

Click here to access/download;Figure;Fig.5.jpg

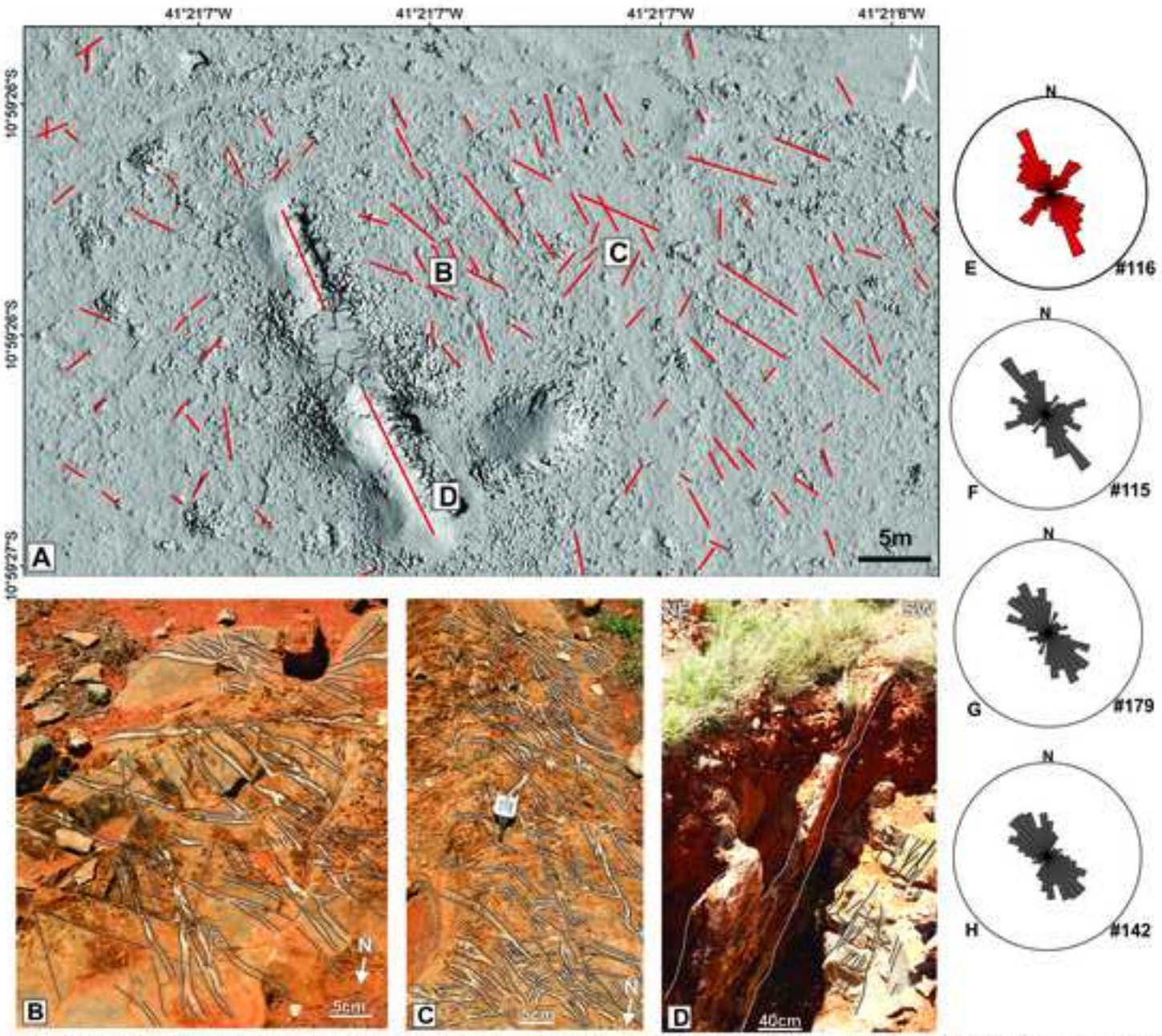

Figure 5. (A) Digital elevation model (DEM) of the Mamonas outcrop (outcrop localization in fig. 2. Mam). Red lines are associated to the structural lineaments; (B)(C) Outcrop view of veins and fractures. (D) Outcrop view of a large vein located in a fault damage zone. (E) Rose diagramm of the identified structural features from the DEM in Fig. 5a; (F) Rose diagramm of the documented veins and fractures displayed in Fig. 5b; (G) Rose diagramm of the documented veins and fractures displayed in fig. 5c; (H) Rose diagramm of the documented veins and fractures displayed in fig. 5d. See Fig. 3 for outcrops location.

Figure 6

Click here to access/download;Figure;Fig.6.jpg

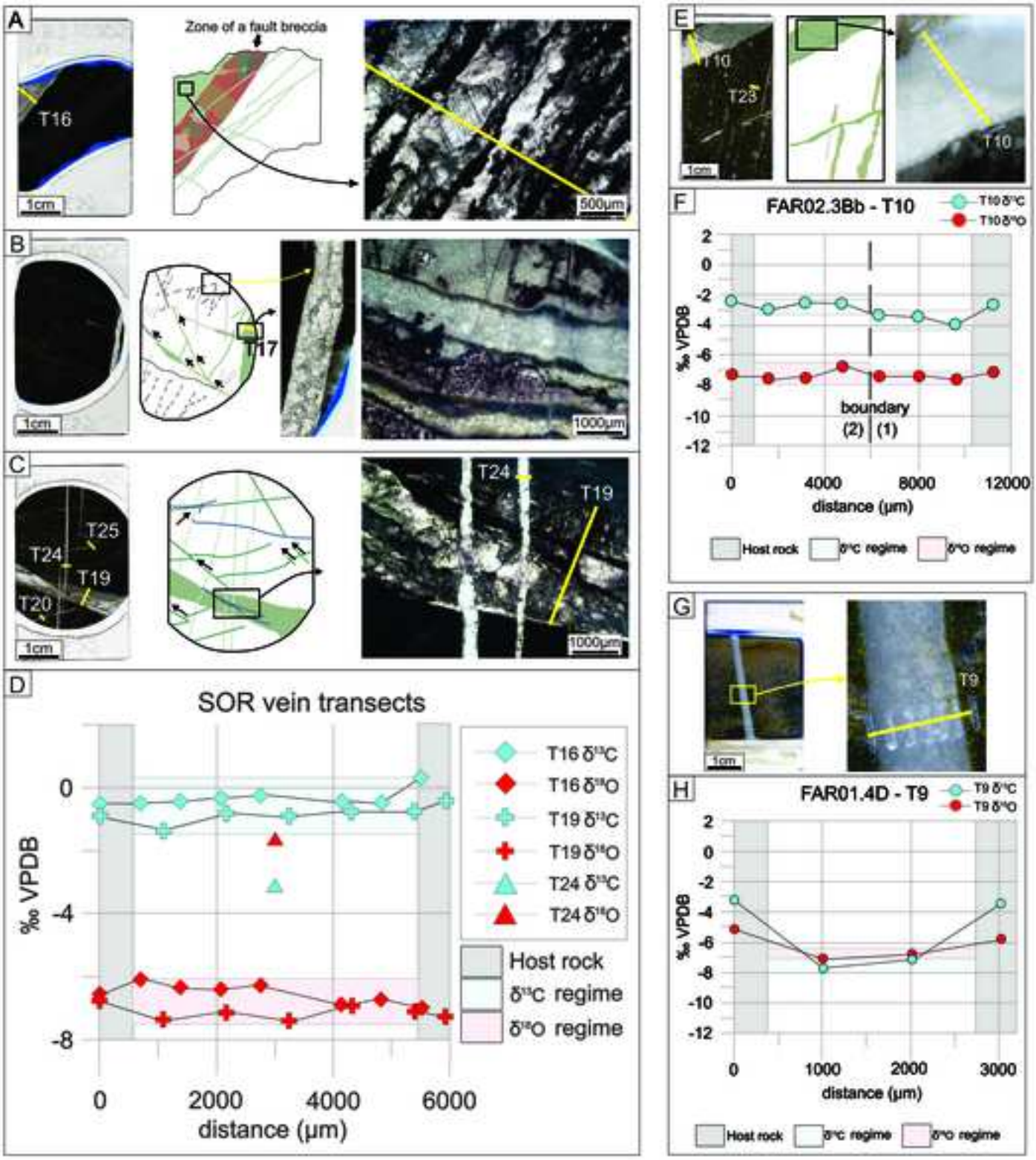

Figure 6. A) On the left, thin section SOR01.2Aa. On the center graphical representation of SOR01.2Aa with veins in green and fault breccia in multicolor. On the right, zoom in on sheeted character of vein T16. B) On the left, thin section SOR01.2Ab. On the center graphical representation of SOR01.2Ab. On the right zoom in on bedding parallel stylolites and NNE-SSW fractures. C) On the left, thin section SOR01.3Aa. On the center Micro map of all present features. On the right, crosscutting of shear fracture T19 and N-S vein T24. D) Stable isotope transects of T16,T19 and T24. E) Thin section FAR02.3Bb. On the center, graphic representation of thin section. On the left, zoom in on transect T10 across two calcite phases including crystallization.F) Transect T10. G) Thin section FAR014D, and zoom in on vein T9 with sampling location including crystallization. H) Transect T9.

Figure 7

Click here to access/download;Figure;Fig.7.jpg

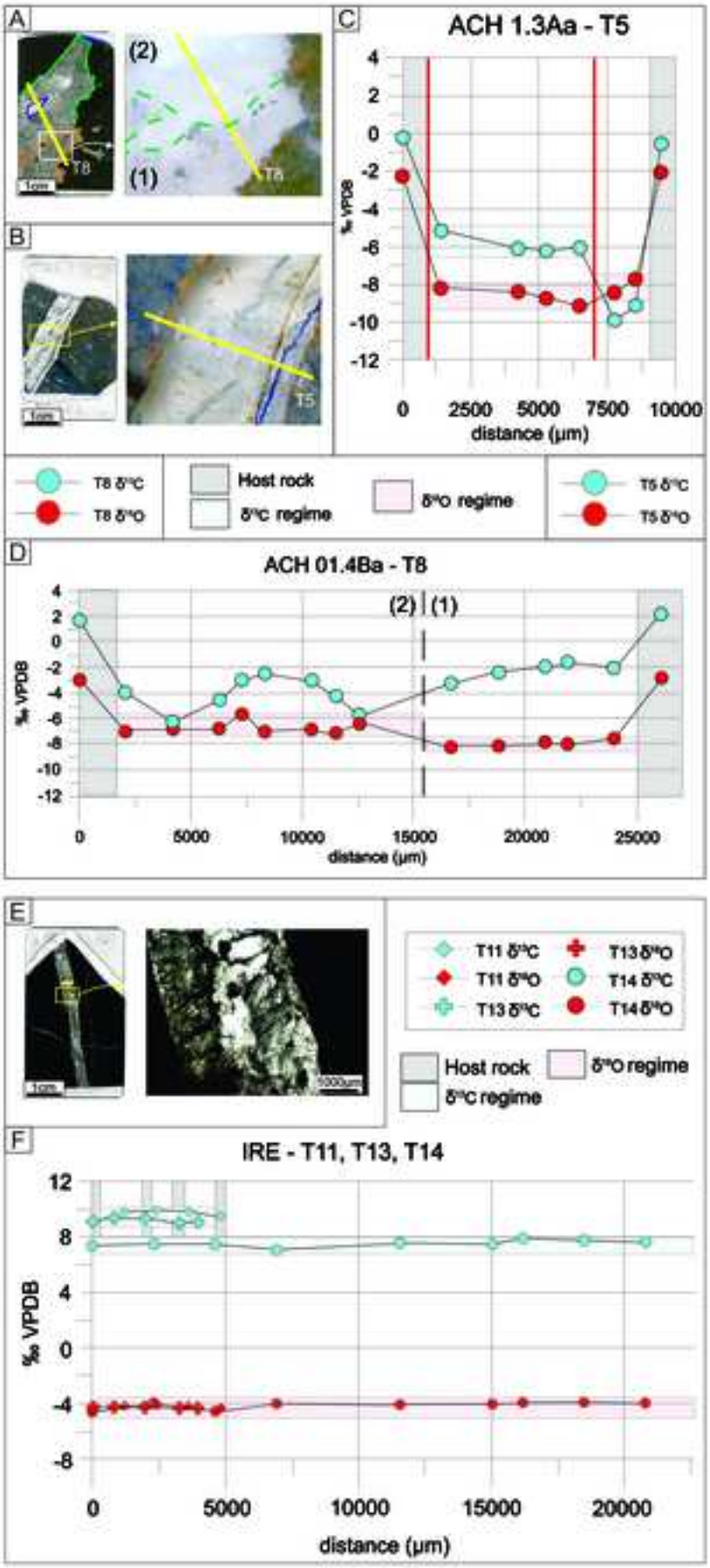

Figure 7. A) Thin section ACH01.4Ba with T8 location and two zones and, zoom in on zone boundary between (1) no host rock remnants and (2) with host rock remnants B) Thin section ACH01.3Aa and, zoom in on transect T5. C) Transect T5. The red lines mark a change in $\delta^{13}C_{VPDB}$ and a new growth plane. D) Stable isotope transect of T8. Note the difference in $\delta^{13}C$. E)Thin section IRE01.2Aa. and, zoom in on vein infill with needle shaped aragonite remnants. F) Stable isotope transects of vein T11, T13 and T14 from IRE. Host rock and vein infill have an almost identical isotope composition.

Figure 8

Click here to access/download;Figure;Fig.8.jpg

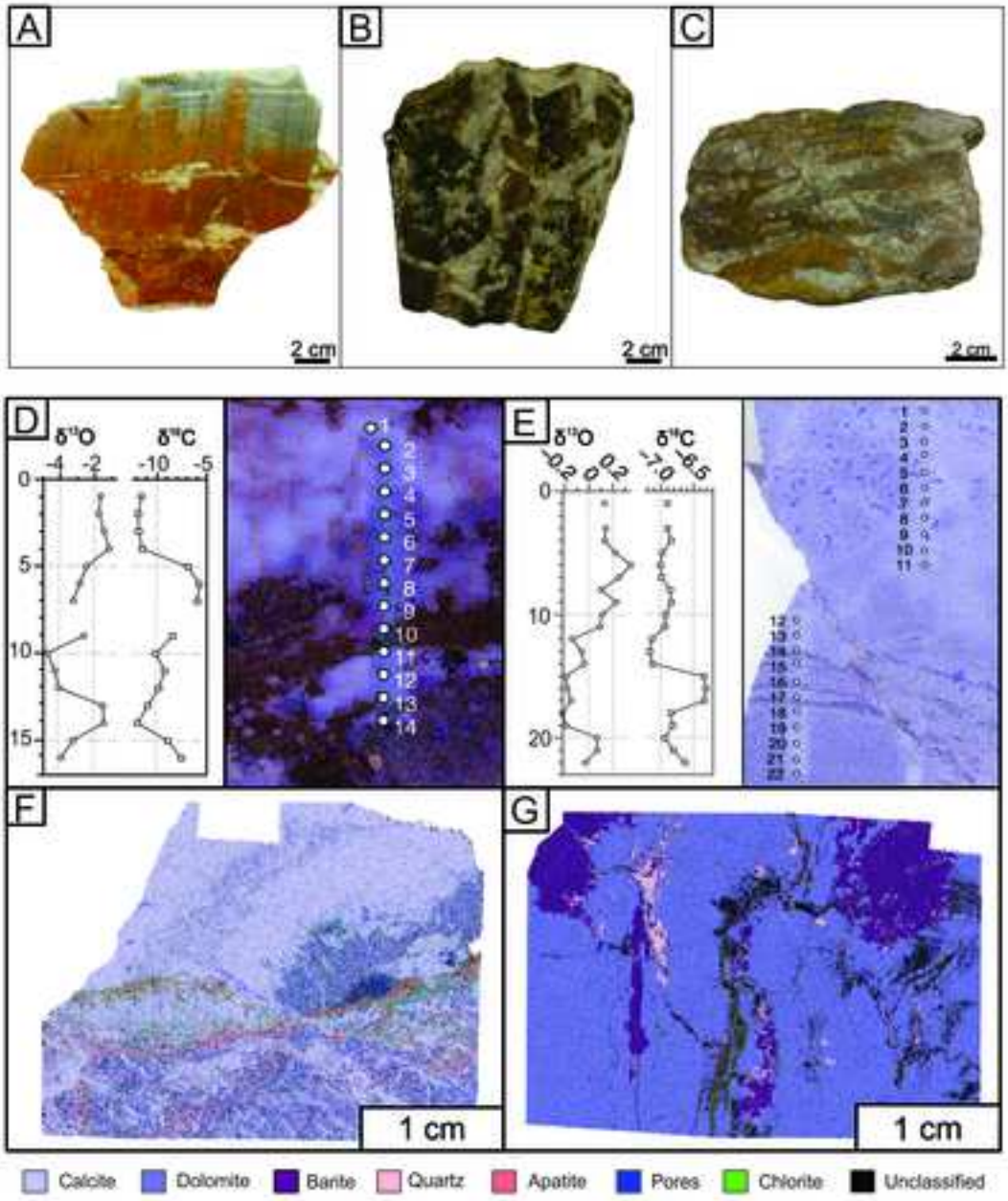

Figure 8. Samples from Melancias area showing the effects of hydrothermal alteration and hydraulic fracturing. A) Carbonate that shows partially preserved primary features grading to a brecciated zone. In the lower part of the sample, the primary features were obliterated by the hydrothermal alteration. B)Vein of carbonate by sucessive precipitation of carbonate and Fe-rich zones. C) Hydralic breccia with clasts of the primary carbonate. D) and E) Thin section from Melancias in which calcite is the main mineral. The diagram also presents $\delta^{13}C$ and $\delta^{18}O$ across profiles. F) and G) QemScan image of samples from Melancias showing the hydrothermal mineralogy made of barite, quartz, illite, and chlorite. Note that these mineras concentrate along fractures.

Figure 9

Click here to access/download;Figure;Fig.9.jpg

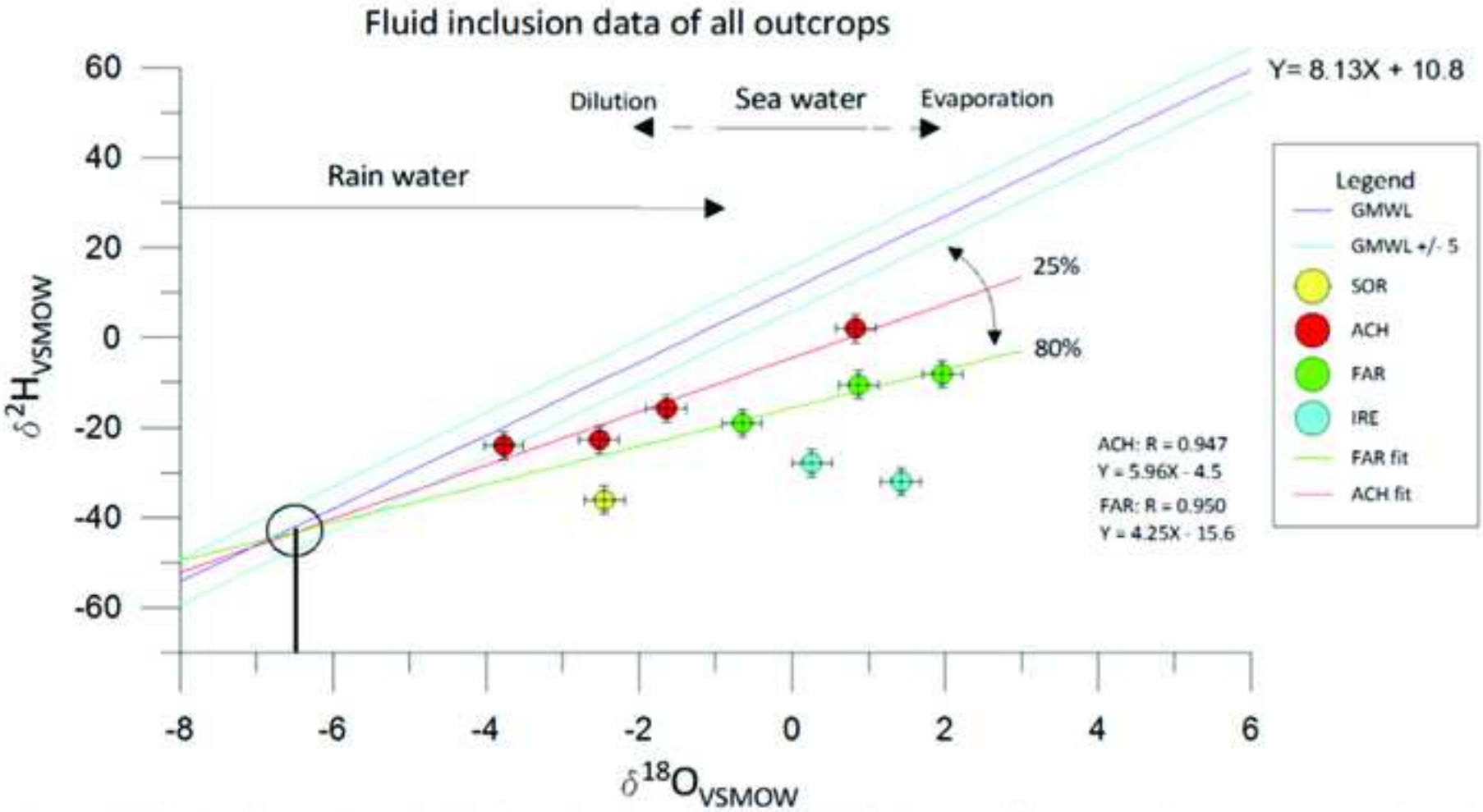

Figure 10. Fluid inclusion data GMWL based on Rozanski et al. (1993). Regions of marine and meteoric waters based on Moore (1989). Sample plot in both meteoric and marine domain. Trend lines of ACG and FAR cross the GMWL on the same point (~-6,5‰ for $\delta^{18}O_{VSMOW}$; -45‰ for δD_{VSMOW}).

Figure 10

Click here to access/download;Figure;Fig.10.jpg

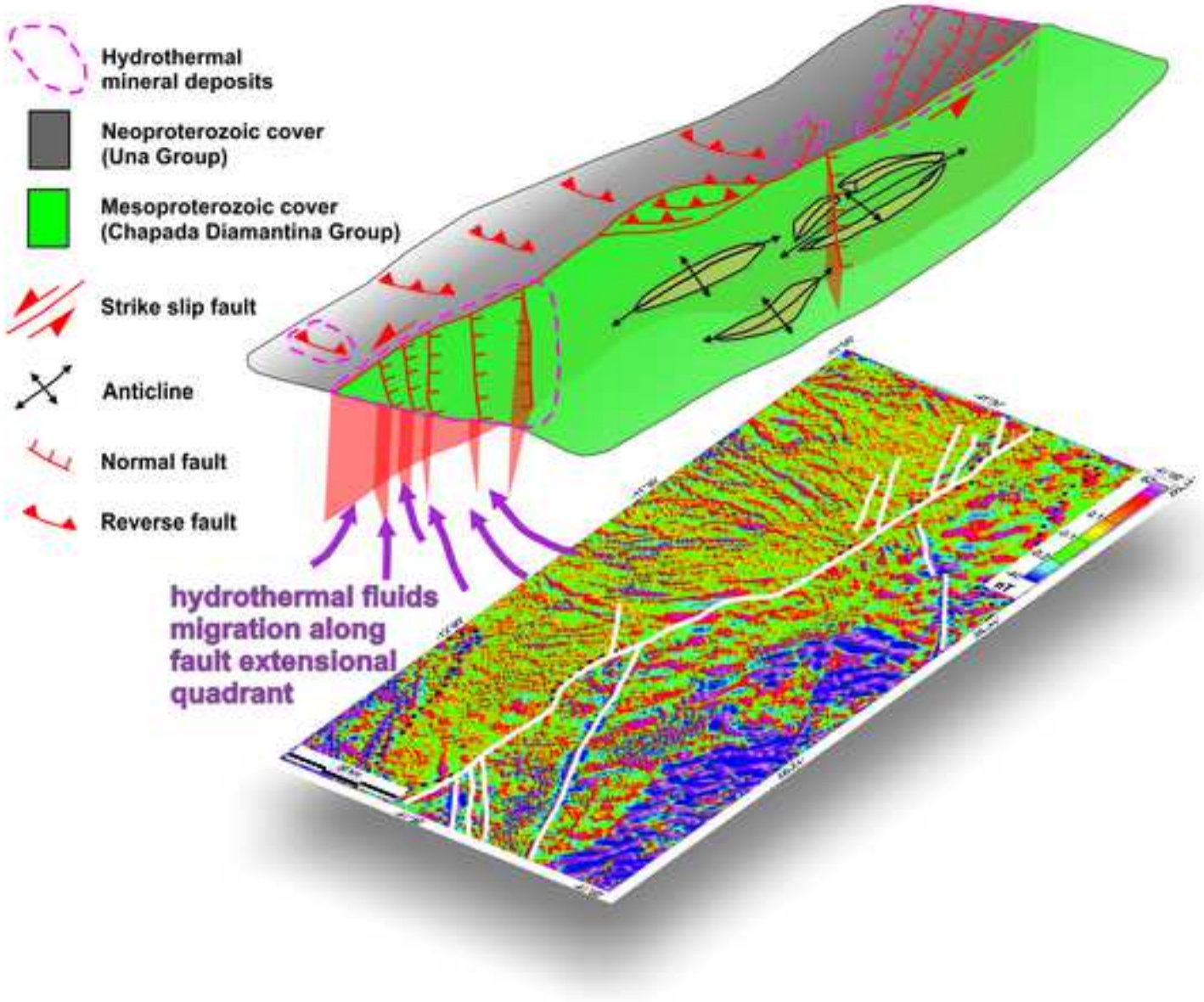

Figure 10. Conceptual model proposed for the study area. Cartoon displaying the current regional scale configuration and the connection with the deep magnetic lineaments.

Figure 11

Click here to access/download;Figure;Fig.11.jpg

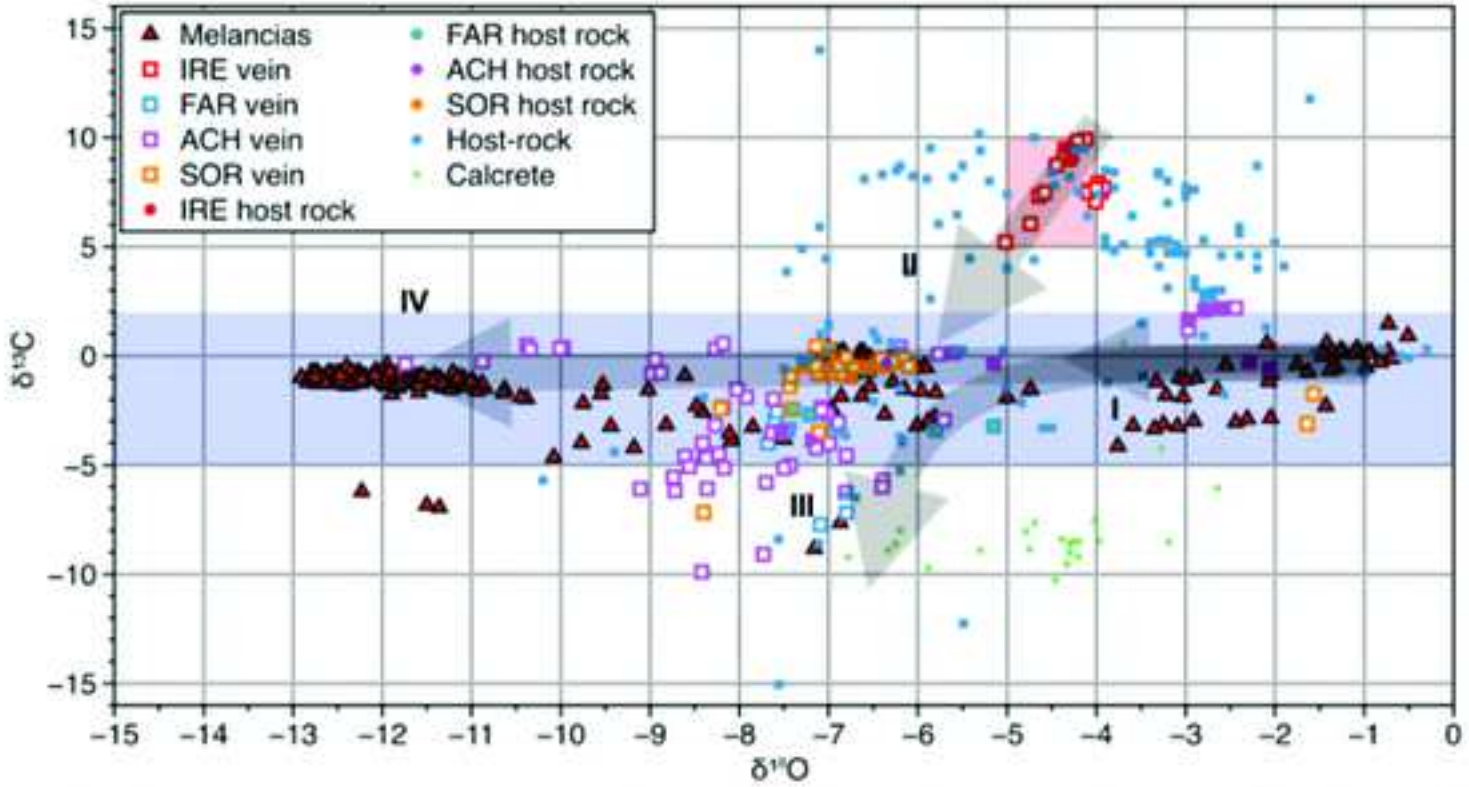

Figure 11. Carbon and oxygen isotopes of samples from the central part of the basin (IRE, FAR. ACH, and SOR) and samples from the Melancias outcrop compared to other published isotope data from the basin. This plot shows different scenarios of isotope evolution: I. Interaction between meteoric fluid and carbonates of the lower stratigraphic section; II. Interaction between meteoric fluid and carbonates of the upper stratigraphic section; III. Low $d^{13}C$ carbonates related to the same fluids responsible for calcrete formation in the area; IV. Carbonates formed by high-temperature fluids that interacted with deep-crustal levels. Host-rock data (Misi and Kyle, 1994; Misi and Veizer, 1998; Borges et al., 2016; Caird et al., 2017); Calcrete data (Borges et al., 2016; Caird et al, 2017).

Table 1: Isotopic composition of carbonates from central part of the basin. IRE; ACH; SOR; FAR. V refers to vein, HR to host-rock, and BREC to breccia.

Achado - ACH				Fazenda Arrecife - FAR				Irecê - IRE				Soares - SOR			
Sample	$\delta^{13}C$	$\delta^{18}O$	V/HR	Sample	$\delta^{13}C$	$\delta^{18}O$	V/HR	Sample	$\delta^{13}C$	$\delta^{18}O$	V/HR	Sample	$\delta^{13}C$	$\delta^{18}O$	V/HR
T3	0.1	-5.6	HR	T9.1	-3.2	-5.2	HR	T11.3	9.8	-4.2	V	T16.1	-0.9	-6.8	HR
T3.2	-4.5	-8.2	V	T9.3	-7.7	-7.1	V	T11.5	9.9	-4.1	V	T16.3	-1.4	-7.4	V
T3.3	-5.2	-7.5	V	T9.5	-7.2	-6.8	V	T11.7	9.8	-4.2	V	T16.5	-0.8	-7.1	V
T3.4	-5.6	-8.7	V	T9.7	-3.4	-5.8	HR	T11.9	9.5	-4.4	HR	T16.7	-0.9	-7.4	V
T3.5	-4.6	-8.6	V	T10.1	-2.5	-7.4	HR	T13.1	9.2	-4.3	HR	T16.9	-0.7	-6.9	V
T3.6	0.1	-5.8	V	T10.3	-3.0	-7.6	V	T13.2	9.4	-4.3	V	T16.11	-0.8	-7.1	V
T4.1	-0.3	-5.2	HR	T10.5	-2.6	-7.6	V	T13.3	9.3	-4.3	HR	T16.12	-0.4	-7.3	HR
T4.2	-0.3	-6.4	HR	T10.7	-2.6	-6.9	V	T13.4	9.0	-4.3	HR	T17.1	0.4	-7.1	V
T4.3	-3.9	-7.2	HR	T10.9	-3.4	-7.5	V	T13.5	9.1	-4.4	V	T17.3	-2.4	-8.2	V
T4.4	-3.4	-7.5	HR	T10.11	-3.5	-7.5	V	T14.1	7.3	-4.6	V	T17.5	-0.1	-6.2	V
T4.5	-0.3	-10.9	V	T10.13	-4.0	-7.7	V	T14.3	7.5	-4.0	V	T19.1	-0.5	-6.6	HR
T4.6	0.4	-10.0	V	T10.15	-2.7	-7.2	HR	T14.5	7.5	-4.6	V	T19.2	-0.5	-6.1	V
T4.7	-0.8	-9.0	V					T14.7	7.1	-4.0	V	T19.3	-0.4	-6.4	V
T4.8	-0.4	-11.7	V					T14.9	6.1	-4.7	V	T19.4	-0.3	-6.4	V
T4.9	0.5	-10.4	V					T14.11	7.6	-4.1	V	T19.5	-0.3	-6.3	V
T4.10	0.3	-10.3	V					T14.13	5.2	-5.0	V	T19.7	-0.5	-6.9	V
T4.12	0.3	-10.0	V					T14.14	7.5	-4.1	V	T19.8	-0.5	-6.7	V
T4.13	0.6	-8.2	V					T14.15	7.9	-4.0	V	T19.9	0.3	-7.0	HR
T5.1	-0.3	-2.3	HR					T14.17	7.7	-3.9	V	T24.1	-3.1	-1.6	V
T5.2	-5.1	-8.2	V					T14.19	7.7	-4.0	V				
T5.4	-6.1	-8.4	V					T12.1	8.7	-4.5					
T5.5	-6.2	-8.7	V												
T5.6	-6.1	-9.1	V												
T5.7	-9.9	-8.4	V												
T5.8	-9.1	-7.7	V												
T5.9	-0.6	-2.1	HR												
T6.1	2.2	-2.6	HR												
T6.2	-4.7	-8.4	V												
T6.3	-5.1	-8.6	V												
T6.5	-2.7	-7.0	BREC												
T6.6	1.2	-3.0	BREC												
T6.7	-2.4	-7.1	BREC												
T6.8	2.2	-2.4	BREC												
T8.1	1.6	-3.0	HR												
T8.3	-4.0	-7.0	V												
T8.5	-6.3	-6.8	V												
T8.7	-4.6	-6.8	V												
T8.8	-3.0	-5.7	V												
T8.9	-2.5	-7.1	V												
T8.11	-3.0	-6.9	V												
T8.12	-4.2	-7.1	V												
T8.13	-5.7	-6.4	V												
T8.17	-3.2	-8.3	V												
T8.19	-2.4	-8.2	V												
T8.21	-1.9	-7.9	V												
T8.22	-1.5	-8.0	V												
T8.24	-2.0	-7.6	V												
T8.26	2.1	-2.8	HR												

Table 2: Isotope data from fluid inclusions of carbonates from the central part of the basin. The temperature was calculated based on the oxygen isotopic composition of calcite and fluid, according to Kim & O'Neil (1997).

Sample	Location	Fluid δD_{SMOW}	Fluid $\delta^{18}O_{SMOW}$	Calcite $\delta^{18}O_{PDB}$	Calcite $\delta^{18}O_{SMOW}$	T in C
ACH01.2Bb T4-1	ACH	-22.7	-2.5	-7.4	23.3	39
ACH01.2Bb T4-2	ACH	-24.0	-3.8	-10.1	20.5	47
ACH01.3Aa T5-1 (left)	ACH	1.9	0.8	-8.6	22.1	66
ACH01.4BaT8-1 (grey)	ACH	-15.7	-1.6	-8.0	22.7	48
IRE01.2Aa T11	IRE	-32.0	1.4	-4.2	26.6	43
IRE01.3Ba T14	IRE	-27.9	0.3	-4.1	26.6	37
SOR01.3Aa T19	SOR	-36.0	-2.5	-6.5	24.3	35
FAR01.4D T9	FAR	-10.5	0.9	-7.0	23.7	56
FAR02.3Bb T10-1 (milky, right)	FAR	-8.2	2.0	-7.6	23.1	67
FAR02.3Bb T10-2 (transparant, left)	FAR	-19.0	-0.7	-7.5	23.1	51